Thesis

Automation and standardization of the 3D workflow in lower limb realignment surgery

S.J.F. van der Linden, BSc.

MSc Student Technical Medicine

Medical Imaging and Interventions

EXAMINATION COMMITTEE

Medical Supervisors:	Dr. R.J.H. Custers
	Dr. N. van Egmond
Technical Supervisor:	Prof. Dr. Ir. C.H. Slump
	H.C. Nguyen, MSc
	Ir. J. Magré
Process Supervisor:	Drs. P.A. van Katwijk

1 ABSTRACT

Introduction: Lower limb deformities can lead to osteoarthritis and impaired function of the knee. An osteotomy can be performed to relieve the injured knee compartment and improve the function. In the challenging cases like large deformities or multiplane deformities, 3D-planning of the osteotomy can increase the correction accuracy. However, this process is not yet standardized and automated in the UMC Utrecht. Therefore, this study aims to develop a standardized and automated process.
Method: Semi-automatic algorithms were developed for deformity analysis, virtual osteotomy planning, and patient specific instrumentation (PSI) design. Intra- and interobserver variability were calculated to validate the deformity analysis algorithm. Moreover, intraclass correlation coefficients were computed for the angles of the lower limb. Furthermore, intra-observer variability was calculated for manual landmark detection. The accuracy of the virtual osteotomy algorithm was calculated by comparing a desired lower limb geometry to the achieved geometry after correction. The PSI algorithm is evaluated by visual inspection and several measurements of the PSI.
Results: Overall, perfect agreement was achieved. The intra-observer variability of manually placed landmarks was higher when compared to semi-automatic algorithm. Mean virtual osteotomy accuracy ranged between 0.01 ± 0.04° and 0.14 ± 0.16°. Visual inspection and measurements of the PSI indicated that all design requirements were met.
Conclusion: In this study the 3D-workflow for the use of 3D technology in osteotomies around the knee was protocolized and automated. This was achieved through the development of several algorithms for deformity analysis, virtual osteotomy, and PSI design.

TABLE OF CONTENTS

2 Introduction

Knee osteoarthritis (OA) is the most common joint disease globally.[1] In 2019, 48,700 new cases of knee OA were diagnosed in the Netherlands.[2] In that year a total of 704,600 knee OA patients were registered in the Netherlands.[2] In 2017, total health care costs associated with knee OA were estimated to be € 488.2 million.[3] The pathogenesis of OA consists of mechanical, metabolic and inflammatory factors which result in alterations of the cartilage, subchondral bone, synovium, capsule, ligaments, and periarticular muscles.[4,5] Knee OA symptoms include pain, reduced range of motion, stiffness, and weakness of the muscles, all leading to an increased disability.[6] Several risk factors are associated with OA such as older age, obesity, female gender, previous knee injury, occupational factors, and varus or valgus malalignment.[4]

The population of OA patients is highly heterogeneous. Possible underlying reason for this heterogeneity is the multiplicity of OA phenotypes, malalignment being one of them.[7] *Figure 1* shows a varus and valgus malalignment of the lower limb. Such a malalignment increases stresses in the medial either the lateral knee compartment.[8] These increased stresses lead to a progression of cartilage loss in the corresponding compartment, resulting in an increased risk of OA.[9–11] A study by Bellemans *et al*. indicates that a constitutional varus is present in 32% of the male knees and 17.2% of the female knees. Whereas a valgus deformity was only present in 2% of the male knees versus 2.8% of the female knees.[12] Malalignment can also be caused by growth or developmental disorders of cartilage or bone. This group of rare disorders are also called skeletal dysplasia, which is a genetic disorder. Skeletal dysplasia can lead to malalignment in multiple planes.[13]

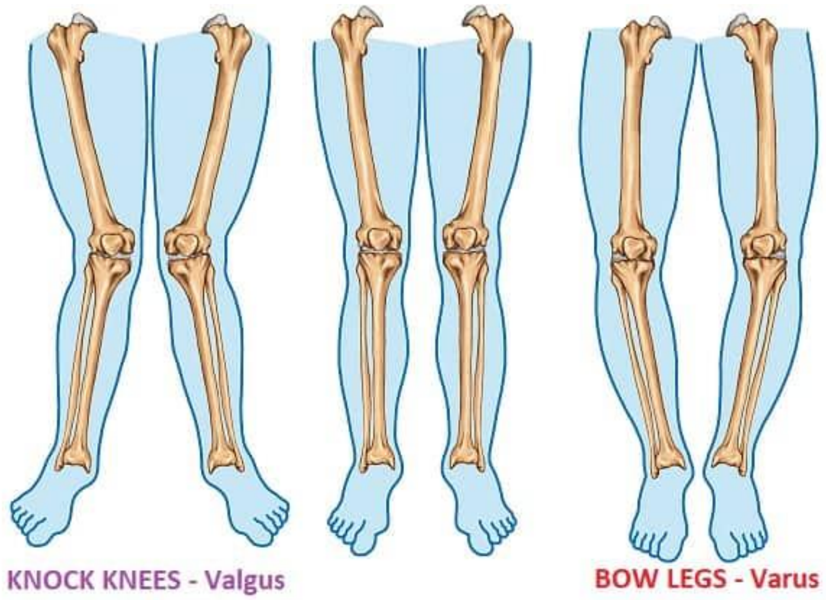

Figure 1: Three types of different lower limb alignments. The left lower limb shows valgus malalignment, the middle a normal stance and the right lower limb has a varus deformity.[14]

Weight-bearing whole leg radiographs (WLR) are considered the gold standard for hip knee ankle angle (HKA) measurements, indicating patients' leg axes.[15,16] The HKA is defined by the angle between the femoral mechanical axis and the tibial mechanical axis. The mechanical axis is the line which connects the centres of the proximal and distal joints of each bone. The mechanical axis of the femur runs from the femoral head centre to the intercondylar notch of the distal femur.[17] The mechanical axis of the tibia runs from the centre of the tibial eminences to the centre of the ankle.[17] Next to the tibial and femoral mechanical axis, the mechanical axis (Mikulicz line) of the whole lower limb is important too, as it shows the load distribution through the knee joint.[18] This axis runs from the femoral head centre to the centre of the ankle, passing the knee joint 4 ± 2 mm medial to the centre.[18] In varus malalignment, this line runs medial of the knee joint, whereas in valgus the Mikulicz line runs lateral of the knee joint. *Figure 2* shows the mechanical axes of the femur, tibia, and the lower limb. The mechanical axis of the femur and tibia are drawn in blue, whereas the Mikulicz line is shown in red. In the right lower limb, a varus deformity can be seen. The left lower limb shows slight valgus malalignment of the lower limb. Normally in healthy adults, a constitutional varus between 1-2° can be observed.[17,19]

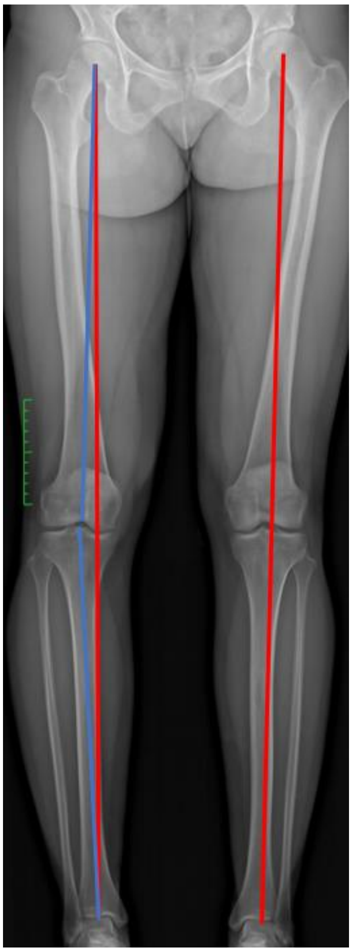

Figure 2: Illustration of a whole leg radiograph. The leg on the left is the right lower limb and the leg on the right is the left lower limb. In red, the Mikulicz lines are displayed. In blue, the mechanical axis of the femur and tibia are shown. A varus deformity of the right lower limb and a slight varus deformity of the left lower limb are present. Adjusted from original image [20]*.*

Besides a deformity in the coronal plane, patients may also present deformities in the sagittal and axial plane. [21,22] In the sagittal plane, tibial slope has an influence on knee joint stability. Sagittal plane deformities can be a result of skeletal dysplasia. A decreased tibial slope is associated with an increased tension on the anterior cruciate ligament (ACL), which leads to an increased risk of rupture.[23] Furthermore, a decreased tibial slope is associated with accelerated knee OA.[24] However, no association with common knee OA was found.[24] The sagittal plane mechanical axis is equal to the coronal plane mechanical axis. This axis, shown in *Figure 2*, runs anteriorly through the knee joint when in full extension.[21] When the knee is roughly in 5-10° flexion, the mechanical axis runs through the knee joint centre of rotation.[21,25] In the axial plane existing deformities are for example tibial torsion and femoral neck anteversion. Tibial torsion is responsible for patellofemoral instability, medial OA, and patellar chondromalacia.[26,27] Furthermore, femoral neck anteversion is associated with slipped capital femoral epiphysis and early hip OA.[28,29]

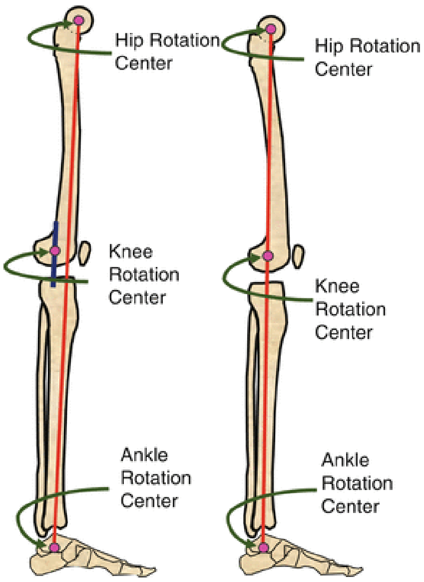

Figure 3: The left lower limb shows the mechanical axis of the lower limb in the sagittal plane in full extension. On the right, the mechanical axis runs through the knee centre of rotation. For this, the knee has to be flexed 5-10°.[25]

Patients with a clinical manifestation of unicompartmental knee OA with malalignment or skeletal dysplasia patients are indicated for a correction osteotomy.[30] An osteotomy shifts the mechanical axis from the injured knee compartment to the healthy knee compartment, which relieves the injured compartment.[8,31,32] An osteotomy preserves the knee joint, while a total knee arthroplasty (TKA) resects the knee joint. TKA is effective in patients with end-stage OA and 60-65+ years of age.[9] Therefore, the ideal osteotomy patients with unicompartmental knee OA are fairly active, rather young (between 40-60 years), a BMI < 30, malalignment < 15°, non-smokers, have a full range of motion, and have an unaffected contralateral knee compartment.[30] Absolute contra-indications for a knee osteotomy are rheumatoid arthritis or a (total) meniscectomy in the compartment intended for weightbearing.[33]

Knee osteotomies can be classified into several techniques, high tibial osteotomy (HTO), distal femur osteotomy (DFO), or a double level osteotomy (DLO).[30] HTO is indicated in patients with a tibial deformity. DFO is indicated for patients with malalignment of the lower limb as a result of a femur deformity.[10] Both HTO and DFO can be performed using open wedge (OW) or a closed wedge (CW) technique.[9] Each technique has its own advantages and disadvantages. OW HTO has a higher correction accuracy, better ten-year survival, wider range of motion, is easier and faster to perform, and the tibiofibular joint is preserved.[34,35] The advantages of CW included that in case of large corrections no autologous iliac bone graft is required, and the posterior slope and limb length do not increase.[9] Furthermore, CW has a decreased likelihood of opposite cortical fractures as compared to OW osteotomies. [34] CW osteotomies are indicated in patients with higher risk of delayed healing or when a higher construction stability is required.[10] Moreover, choice for opening wedge and closing wedge osteotomy can be based on leg length discrepancy. *Figure 4* shows all types of osteotomies around the knee. The MOW DFO is not performed in the UMCU due to the increased chance of complications.

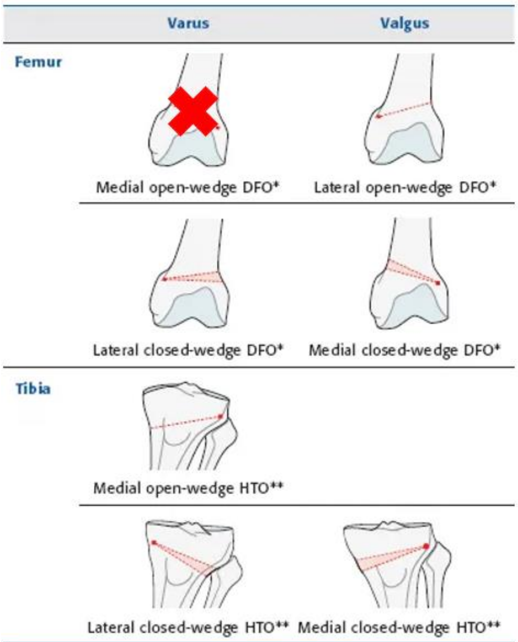

Figure 4: The various type of distal femur (DFO) and high tibial osteotomies (HTO). The red lines show the cutting lines of the osteotomy. The red areas are the wedges which are removed during a closed-wedge osteotomy. Medial opening wedge DFO is not recommended. Adapted from original image.[36]

Adequate pre-operative planning of the surgical correction is important. Pre-operative planning is currently performed on antero-posterior weight bearing whole leg radiographs (WLR). This 2D approach can lead to overlooked sagittal and transversal deformities. Moreover, multiplane deformities affect measurement accuracies in the coronal plane.[37–39]

A large systematic review by Van den Bempt *et al.* found that eight out of 14 studies reported a success rate below 75% using the conventional osteotomy procedure.[40] Success rate was defined as percentage of procedures falling within the proposed accuracy range (AR). An interval including al ARs of the studies in the review ranges from 3° of varus to 8° of valgus.[40] This shows that achieving the planned correction per-operatively remains difficult.[41]

Planning the osteotomy using three-dimensional (3D) visualization from computed tomography (CT) images increases the accuracy.[41,42] 3D-planning and the use of personalized surgical instruments (PSI) enables the translation of the pre-operative planning into the per-operative setting without computer-assisted surgical navigation.[41,43,44] A final advantage of PSIs is the reduced operating time, reduction of total fluoroscopic images, and shortening of the surgical learning curve.[44]

In the challenging cases (large deformities or multiplane deformities), 3D-planning of the osteotomy can increase correction accuracy.[41,42] The first step in the current 3D-workflow in the University Medical Center Utrecht (UMCU) is acquisition of CT-data, followed by segmentation and deformity analysis. During deformity analysis, landmarks on both the femur and tibia are located. Using these landmarks, several axes and angles are calculated. in 3D. After deformity analysis, the correction is planned in the 3-matic (Materialise, Version 16.0, Leuven, Belgium) environment and eventually translated into a 3D-printed PSI.

In the current clinical practice in the UMCU, the workflow of performing 3D deformity analysis, creating a pre-operative planning, and designing a PSI is not standardized yet. Standardization is required to reduce variability in treatment, improve correction accuracy and reduce preplanning effort.[45] This can be achieved by protocolizing and automating the 3D-workflow. Automation reduces the amount of user input, whereas protocolization reduces input variability. Both lead to a minimization of intra- and interobserver variability. The aim of this study is to protocolize and automate the 3D-workflow for the use of 3D technology in osteotomies around the knee in the UMCU. This aims to reduce the intra- and interobserver variability, add a quality control to the entire process and reduce the total time needed to design PSI for the use in lower limb osteotomies.

3 OBJECTIVES

Currently, several projects on 3D technology in deformity analysis and personalized surgical instrument (PSI) development have been conducted at the UMCU. However, the entire process from CT-scan to deformity analysis, virtual osteotomy planning, and PSI design has not been standardized yet. The main objective of this study is to protocolise and to automate the entire 3D-workflow in lower limb malalignment care.

First, 3D deformity analysis has only been partly studied and implemented for the femur and tibia. This project will further develop and implement methods for 3D analysis of these two bones. The developed methods must be validated before implementing them into the clinical care of patients.

The second objective of this study is protocolizing the translation of the deformity analysis into pre-operative planning. Pre-operative planning of osteotomies is based on measured bone geometry, combined with patient and surgeon demands. Based on these variables, the algorithm must perform a virtual osteotomy. The algorithm will propose a surgical correction angle, based on the osteotomy site, hinge location, and location of plate fixation.

Third is the development of the PSI. This part of the project aims to develop a clinically viable semi-automatic algorithm for the creation of PSIs. This method must include the six current types of lower limb osteotomies. Standardization and automatization are important for clinical processing time, accuracy, and repeatability.

Finally, the implementation of the entire 3D-workflow into clinical care must be validated. The goal is to standardise and automate the process of performing corrections in multiple planes.

4 RESEARCH QUESTIONS

Is an automated, protocolized, and standardized 3D workflow in lower limb realignment surgery clinically achievable?

- What is important and needed for reliable and repeatable semi-automated measurements on 3D lower limbs?
  - What are the intra- and interobserver variabilities of the semi-automatic deformity analysis algorithm?
  - What is the accuracy of the deformity analysis script as compared to manual localisation of all landmarks?
- What is the accuracy of the achieved virtual osteotomy correction by the algorithm as compared to the desired geometry?
- What is necessary to standardize, optimise, and automate the design process of a PSI for high tibial and distal femur osteotomies?

5 METHOD

5.1 METHOD 3D DEFORMITY ANALYSIS

5.1.1 Study population

The 3D deformity analysis section of this project included fifty lower extremity CT-scans. The indications for the CT-scans were not related to the orthopaedic field. All scans were collected from the UMCU. database, of which the included patients signed a broad informed consent for the use of their imaging materials. A separate approval of the Medical Ethical Committee of the UMCU for conducting this study was not necessary for this study.

CT-scans were acquired using Philips iCT scanner or Philips Brilliance 64 (Philips Medical Systems, Best, The Netherlands). The following settings were used: tube voltage of 120 kVp and tube current of 150 mAs. The slice thickness was 1.0 mm. The reconstructions were made using a field of view including both legs with a matrix size of 512x512 pixels and a slice increment of 0.7 mm. Voxel sizes for the systems were 0.63 mm × 0.63 mm × 1.00 mm and 0.98 mm × 0.98 mm × 1.00 mm. Both systems applied the iDose reconstruction system.

Sample size calculations were performed based on estimations of the ICC as described by Walter *et al.*.[46] For calculation an excepted reliability of ICC was 0.97, minimal acceptable reliability was 0.90, the significance level was 0.05, power was 80%, and number of raters was three. This resulted in a minimal sample size of seventeen subjects.

5.1.2 Methods

All CT-scans were segmented using Mimics 24.0 (Materialise, Leuven, Belgium). The segmentation was based on the CT bone threshold of 226 Hounsfield units as applied in the advanced bone segmentation tool. The segmentations were visually inspected, and manual adjustments were made if required. Segmentation resulted in a 3D-models of the lower limbs (femur, tibia, and fibula). For deformity analysis, several angles of the femur and tibia were measured. The femur angles include the lateral proximal femur angle (LPFA), mechanical lateral distal femur angle (midface), and femoral rotation. The definitions of these angles are displayed in *Table 2*. The angles of the femur and their definitions are based on 11 landmarks as described by Fürmetz *et al.*.[47] The definitions of the landmarks are shown in *Table 1*. The angles of the tibia (*Table 3)* include the mechanical medial proximal tibial angle (mMPTA), mechanical lateral distal tibial angle (mLDTA), posterior proximal tibial angle (PPTA), and tibial rotation. These angles are based on 10 landmarks, shown in *Table 4*.[47] *Figure 5* and *Figure 6* show all landmarks as described in the tables.

Table 1: Landmarks of the femur with their definitions

Landmark	Definition
Femoral hip centre (FHC)	Midpoint of the femoral head
Femoral notch point (FNP)	Most cranial point of the femoral notch
Femoral neck centre (FNC)	Midpoint on the line across the narrowest part of the femoral neck
Femoral condyle medial (FCM)	Most medial point of medial condyle
Femoral condyle lateral (FCL)	Most lateral point of lateral condyle
Transepicondylar midpoint (TEM)	Midpoint between FCM and FCL
Tip of greater trochanter (TGT)	Most cranial point of the greater trochanter
Femoral lateral condyle distal (FLCD)	Most caudal point on the lateral condyle
Femoral medial condyle distal (FMCD)	Most caudal point on the medial condyle
Femoral lateral condyle posterior (FLCP)	Most dorsal point on the lateral condyle
Femoral medial condyle posterior (FMCP)	Most dorsal point on the medial condyle

Table 2: Angles and axes of the femur with their definitions and planes

Angle or axis	Definition	Plane
Mechanical femoral axis (MFA)	FHC-FNP	Coronal and sagittal
Mechanical lateral distal femoral angle (mLDFA)	Angle between MFA and the axis FLCD-FMCD	Coronal
Lateral proximal femur angle (LPFA)	Angle between MFA and the axis FHC-TGT	Coronal
Femoral torsion	Angle between axis FHC-FNC and FLCP-FMCP	Transversal

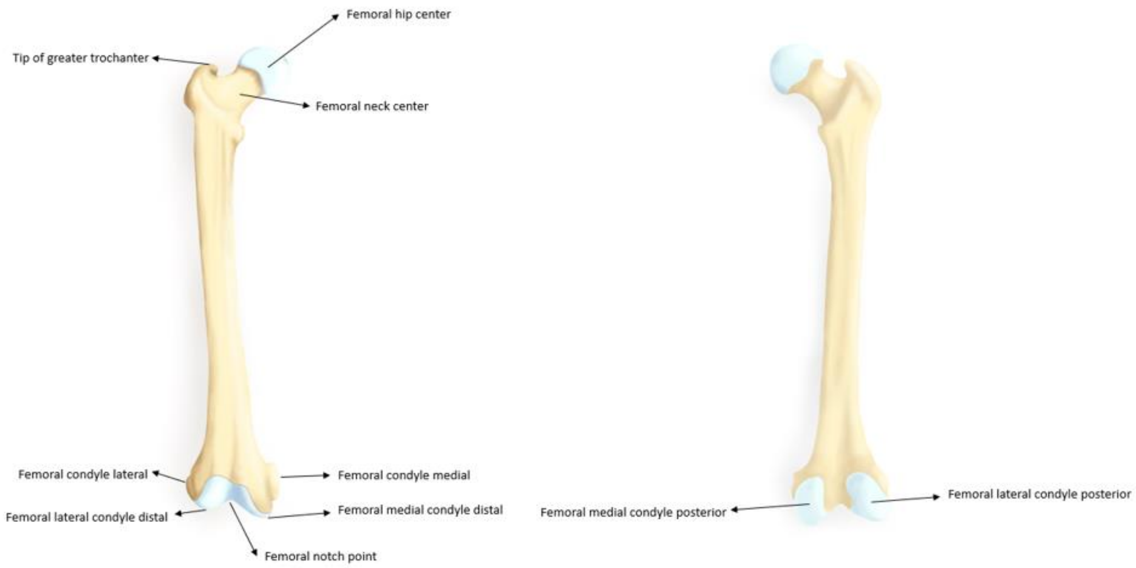

Figure 5: Anterior and posterior view of the femur. Ten landmarks required by the algorithm are shown. The transepicondylar midpoint, which is in the middle of the axis between the medial and lateral epicondyle, is not displayed. Adjusted from original image.[48]

Table 3: Landmarks of the tibia with their definitions

Landmark	Definition
Tibial knee centre (TKC)	Midpoint of the medial and lateral intercondylar tubercle
Tibial ankle centre (TAC)	Midpoint of the tibial plafond area
Medial intercondylar tubercle	Protrusion on the intercondylar eminence on the medial side
Lateral intercondylar tubercle	Protrusion on the intercondylar eminence on the lateral side
Tibial medial condyle posterior (TMCP)	Most dorsal and cranial point on the medial condyle
Tibial lateral condyle posterior (TLCP)	Most dorsal and cranial point on the lateral condyle
Tibial medial malleolus (TMM)	Most medial point of the medial malleolus
Tibial lateral malleolus (TLM)	Most lateral point of the lateral malleolus
Posterior cruciate ligament insertia (PCL insertia)	Posterior aspect of the tibial plateau, 1 cm distal to the joint line
Medial border of tibial tuberosity	A point on the border of the medial side of the tibial tuberosity

Table 4: Angles of the tibia with their definition and plane

Angle	Definition	Plane
Medial proximal tibial angle (MPTA)	Angle between MTA and axis TLCL - TMCM	Coronal plane
Mechanical lateral distal tibial angle (mLDTA)	Angle between transmalleolar axis and mechanical tibial axis.	Coronal plane
Posterior proximal tibial angle (PPTA)	Angle between proximal tibial plateau plane and mechanical tibial axis	Sagittal plane
Tibial torsion	Angle between axis TLCP-TMCP and TLM-TMM	Transversal plane

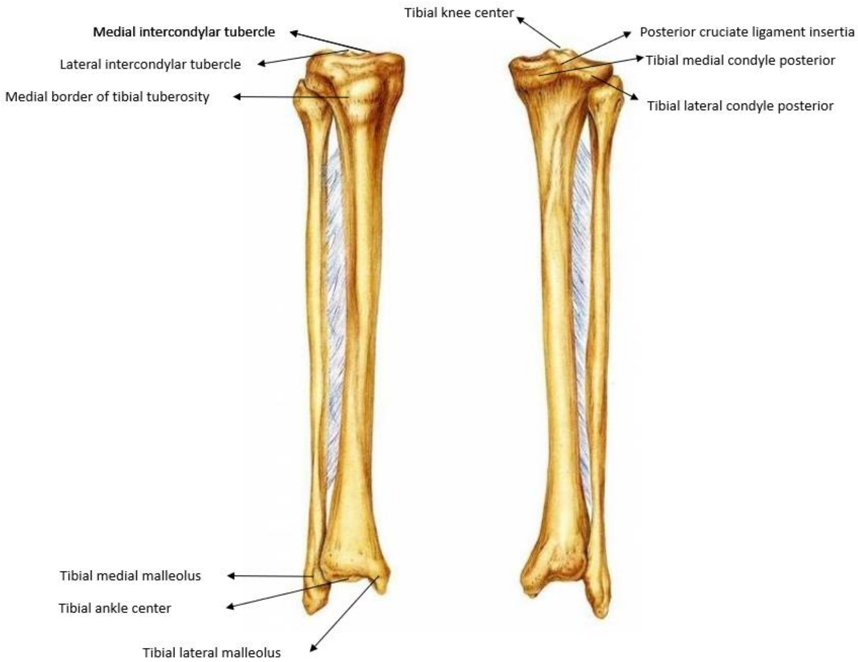

Figure 6: Anterior and posterior view of the tibia. All landmarks required by the algorithm are shown. Adjusted from original image.[49]

5.1.3 Requirements deformity analysis algorithm

Semi-automatic algorithms were developed for both the tibia and the femur to detect bony landmarks. The algorithms must fulfil several requirements, namely:

- Reduce the time needed to find all bony landmarks and angles as compared to manual selection
- Orthopaedics department staff, i.e.: Technical Physicians, Biomedical Engineers, or Technical Medicine students, should be able to work with the algorithm
- Must be usable on 95% of all patients
- Must be capable of performing measurements on both the right and left lower limb
- Minimal manual actions should be conducted
- Have an excellent reproducibility and repeatability. Intra- and interobserver ICCs in other studies range from 0.90 to 0.99.[50–54]

5.1.4 Algorithm femoral landmarks and angles

The developed algorithm for finding the femoral bony landmarks requires four manual steps by the user. First the spherical part of the femoral head is marked, next the medial and lateral epicondyle must be selected globally (within 5 mm). Finally, the trochlea is marked. Based on this information, the semi-automatic algorithm finds all angles and landmarks as listed in *Table 1 and 2*.

Femoral hip centre

Based on the marked spherical part of the femoral head, a sphere is fitted. The marked part should go around the entire femoral head completely, as displayed in *Figure 7*. The FHC is defined as the centre of this sphere, as shown in *Figure 7*.

Femoral neck centre

To obtain the FNC, the radius of the sphere is iteratively enlarged by 0.1 mm. An intersection between the sphere and femoral neck is made and the volume of this intersection is calculated. This is done for the entire femoral neck. The centre of gravity of the intersection with the smallest volume is indicated as the FNC. The line between the FHC and FNC represents the femoral neck axis, which is shown in *Figure 7*.

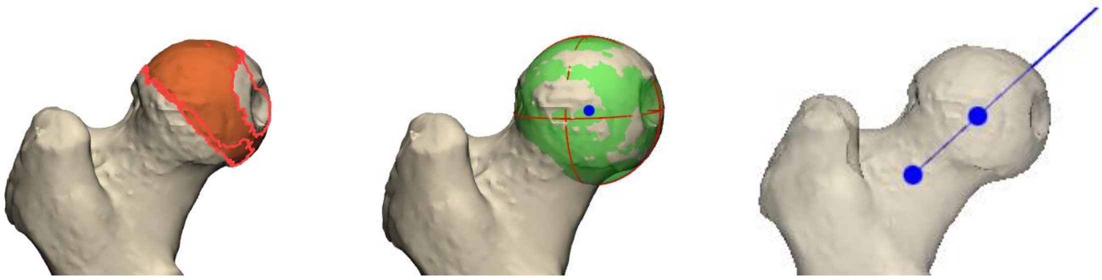

Figure 7: The left image shows the marked part of the femoral head. In the middle image the sphere is fitted based on the marked area. The femoral hip centre and femoral neck centre which together form the femoral neck axis are displayed on the right.

Lateral and medial femoral epicondyle

First the user indicates the global location of the lateral femoral epicondyle (FCL) and medial femoral epicondyle (FCM). Between these two points, a cylinder with a radius of 5 mm is designed. This 5 mm radius was based on the study of Fürmetz *et al*. which observed mean intra- and interobserver error for manual landmark selection of less than 5 mm.[47] Using an extrema analysis in the z-direction of the cylinder, the outermost points of the medial and lateral condyles are found. Between these two points a line is drawn which indicates the transepicondylar axis (TEA). The centre of this axis is the transepicondylar midpoint (TEM). The TEM and epicondyles are displayed in *Figure 8*.

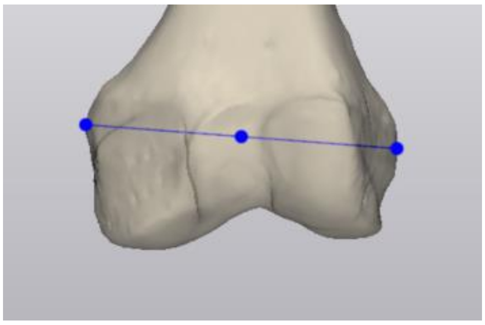

Figure 8: The transepicondylar axis between the medial and lateral epicondyle. The middle of this axis is the transepicondylar midpoint.

Femoral notch point

The femoral notch point (FNP) is located by marking the trochlea. The algorithm then created an inertia axis based on the marked area. Two points on the y-axis of the inertia axis and the FHC are used to create a plane. Next the contour of the femur in this plane is drawn. Then, the most distal point of this contour is found by performing an extrema analysis in the direction of a line running from the FHC to the TEM. The FHC and FNP together form the mechanical axis of the femur *(Figure 9*).

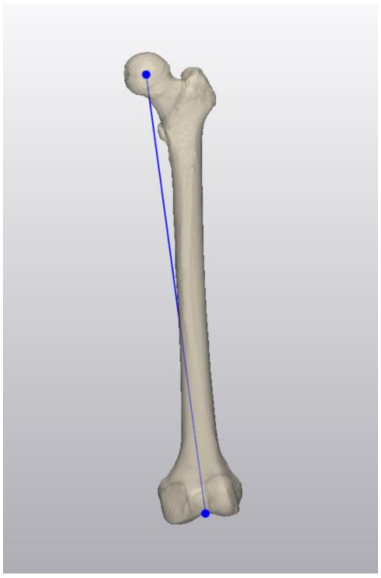

Figure 9: The mechanical axis of the femur, which is the line between the femoral hip centre and femoral notch point (FHC-FNP).

Tip of greater trochanter

The tip of the greater trochanter (TGT) is obtained by drawing a line between the FCM and the FNC. Next, the femoral head and femoral neck are subtracted from the femur. Extrema analysis is then used to find the TGT in the direction of the line drawn before. An axis between these two points is then constructed as displayed in *Figure 10*.

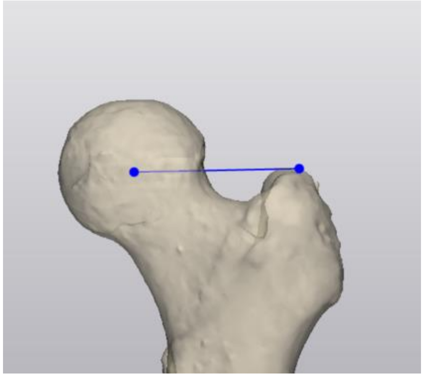

Figure 10: The axis running between the femoral hip centre and the tip of the greater trochanter (FHP-TGT).

Posterior points medial and lateral condyle

First, the mechanical axis is constructed by drawing a line between the FHC and the FNP. Perpendicular to this line a plane is constructed. After this, the femur is split in a proximal and distal part by creating a plane between the FHC and the TEM. Next, the distal femur is split by a midplane between the epicondyles. Lastly, the medial and lateral distal femur are split into an anterior and posterior part. This is done by a plane perpendicular to the first plane, which runs from the medial epicondyle to the lateral epicondyle. Extrema analysis, which calculates the outermost points, is performed perpendicular to this last plane to find the posterior points. An overview of all planes is given in *Figure 7*.

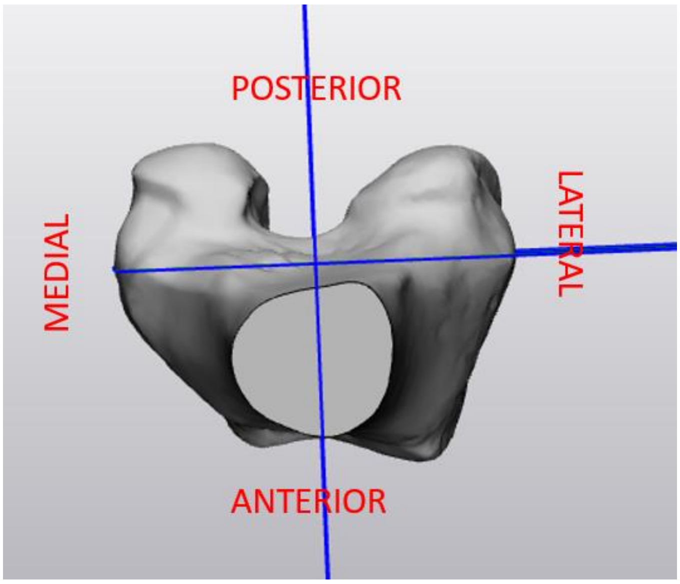

Figure 11: Planes dividing the distal femur in four parts, namely: anteromedial, anterolateral, posteromedial, posterolateral.

Distal points medial and lateral condyle

The distal points are found using the extrema analysis in the direction of the mechanical axis. For this, the left and right distal femur as described before are used.

Transversal, coronal, and sagittal plane

The transversal plane is constructed in the FNP. This plane is perpendicular to the mechanical axis. The coronal plane runs perpendicular to the transversal plane and between the medial and lateral epicondyle. Lastly, the sagittal plane is perpendicular to the transversal and coronal plane. *Figure 8* shows the coronal, sagittal and transversal plane of the femur.

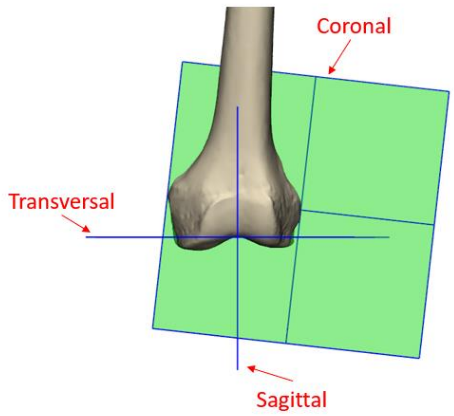

Figure 12: Orientation of the planes around the femur. The coronal, sagittal and transversal planes are displayed.

5.1.5 Tibial landmarks

The landmarks of the tibia are also found by the algorithm with four manual steps as input. First the distal and proximal tibial plateau are marked. Then the location of the tibial posterior cruciate ligament attachment is marked. Finally, the user indicates a point medial to the tibial tuberosity. With this method all angles and landmarks as described in *Table 3 and 4* are found.

Tibial ankle centre and distal tangent

The tibial ankle centre (TAC) is found by marking the distal tibia plateau. Next, the centre of gravity of the marked area is calculated. This is the tibial ankle centre. Furthermore, the distal tangent is calculated by fitting a line to the marked surface. The TAC and distal tangent are displayed in *Figure 14*.

Proximal tibia plateau

To find the proximal tibia plateau, the medial and lateral plateau are marked. Next, a plane is fitted based on the marked areas.

PCL insertia

This landmark is obtained by marking the area where the PCL attaches to the tibia. The point is found by calculating the centre of gravity of the marked area.

Medial tuberosity and Akagi's line.

This point is manually selected by placing a point medial to the tibial tuberosity. The algorithm displays a curvature analysis of the tibia, which highlights the transition between tuberosity and tibia. The line between the PCL insertia and medial tuberosity is the Akagi line, which is shown in *Figure 13*.

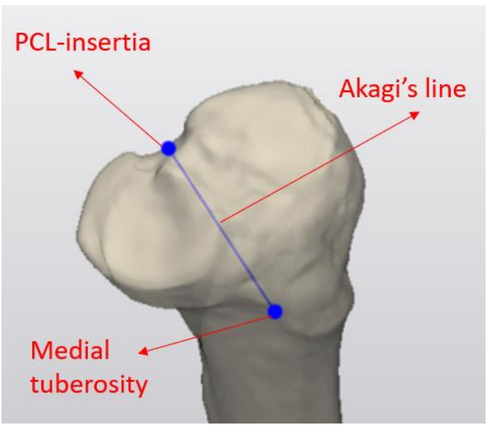

Figure 13: The Akagi line runs between the PCL insertia and medial tuberosity.

Lateral and medial malleolus
First, a cylinder is fitted to the marked area of the distal tibia plateau. The radius of this cylinder is then reduced by 1 mm. Next, an intersection between the two cylinder walls and the medial and lateral malleoli is made. This intersection between cylinder walls and malleoli, results in transversal slices of both the lateral- and medial malleolus. The centre of gravity of the malleolar slices are computed by the algorithm. The computed points are the landmarks of the malleoli *(Figure 14*).

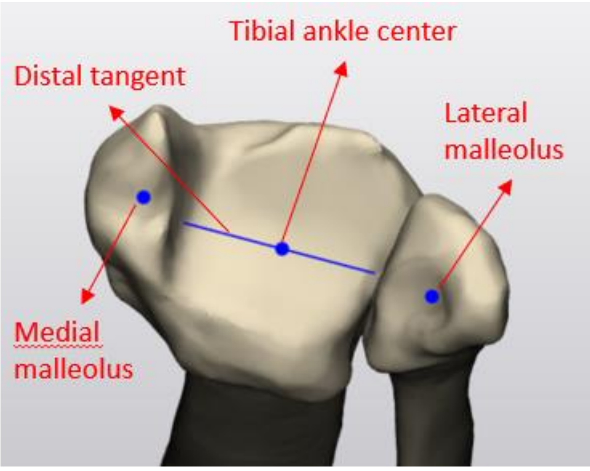

Figure 14: The two outer points are the centres of the medial and lateral malleolus. The middle point is the tibial ankle centre. Furthermore, the distal tangent is displayed.

Eminentia and tibial knee centre
To find the eminentia, a plane is constructed between the PCL insertia and the medial tuberosity. The plane is perpendicular to the proximal tibia plateau. Using this plane, the tibia is cut in a lateral and medial part. Next, a temporary mechanical axis of the tibia is constructed between the centre of this plane and the TAC. The eminentia are found by computing an extrema analysis for the lateral and medial tibia in the direction of this mechanical axis. The user then visually inspects the location of the landmarks. If the landmarks are not located correctly, the user is prompted to manually locate the eminentia. A cylinder in the direction of the temporary mechanical axis is constructed on the manually selected points. This cylinder is intersected with the eminentia. Again, an extrema analysis is computed for these intersections in the direction of the temporary mechanical axis. Finally, a midplane is constructed between the two eminentia. The origin of this plane is the tibial knee centre (TKC).

Anatomical axis
The anatomical axis of the tibia is the line drawn between the centre of the tibial shaft at 1/3 and 2/3 of the total length.[47] The length of the tibia is equal to the length of the mechanical axis. A plane perpendicular to the mechanical axis is created at 1/3 and 2/3 of this length. The plane is then intersected with the tibia. The centres of gravity of these intersections are then used to draw the anatomical axis.

Transversal, sagittal, and coronal plane
The transversal plane is placed at the TKC and is perpendicular to the mechanical axis. The sagittal plane is perpendicular to the transversal plane and runs through the medial tuberosity and the PCL attachment point. Finally, the coronal plane is perpendicular to those two planes and its centre is located at the TKC. *Figure 15* shows the coronal, sagittal and transversal plane of the tibia.

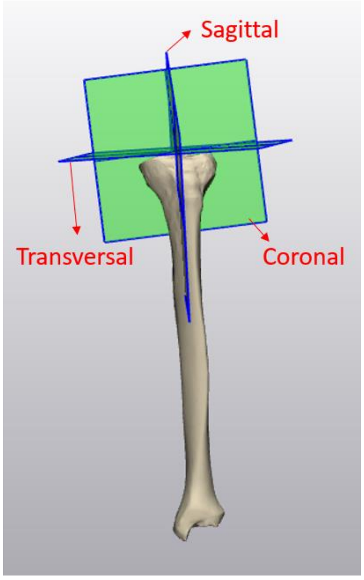

Figure 15: The planes describing the direction of the tibia. Shown are the coronal, sagittal and transversal plane.

Tibial plateau coronal and sagittal tangent
The coronal tangent is the line that is formed by the intersection of the coronal plane and the proximal tibia plateau plane. The sagittal tangent is the intersection of the sagittal plane and the proximal tibia plateau plane. The coronal and sagittal tangent are shown in *Figure 16*.

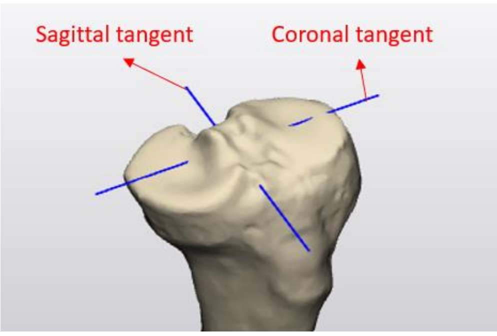

Figure 16: Coronal and sagittal tangent of the tibia plateau.

Lateral and medial posterior points
The posterior points are found in the area between the top of the fibula and just below the proximal tibia plateau. First, the tibia is split in a lateral and medial part. Next, the most posterior points of the lateral, medial, and distal tibia are found by computing an extrema analysis in the direction perpendicular to the coronal plane. These three points are then used to create a posterior plane, which is used to cut the tibia. This results in three small parts of the tibia. Iteratively, the three points are relocated. This is done until the volume of the three parts is less than 0.1 mm^3. The location of the points on the lateral and medial part of the tibia are then indicated as the most posterior points.

5.1.6 Manual landmark registration

Besides semi-automatic landmark detection using the 3D deformity analysis script, manual registration can be performed. The manual registration was performed as described by Fürmetz *et al.*.[47] This was done to compare semi-automatic and manual registration. In total ten lower limbs were analysed. Manual registration was visually compared to semi-automatic registration for all landmarks. Landmarks of both methods were projected on a single lower limb. The landmarks were then assigned to one of three groups, namely: semi-automatic registration most accurate, manual registration most accurate and landmark could not be assigned to one of two other groups.

5.1.7 Statistical analysis

Ten segmentations were used to create the algorithm and were therefore excluded from analyses. In total, forty segmentations of both lower limbs were included for statistical analysis. The intra- and interobserver variability were calculated for all landmarks and angles of both the femur and tibia. One observer (SL) performed all measurements twice, with two weeks in between, to compute intra-observer agreement. This resulted in a total of 160 measurements of both the femur and tibia. Two researchers of the 3D Lab UMCU (JM, CN) with several years of experience in deformity analysis performed measurements once for interobserver variability. This resulted in another 160 measurements of both the femur and tibia. In total 240 measurements were used to calculate interobserver variability. For the landmarks, the mean Euclidian distance and the standard deviation was calculated. Measurements for the left and right femur were combined to find a final mean Euclidian distance and standard deviation. For the angles, the absolute difference and standard deviation were computed. Besides these angles, an additional angle was calculated. This angle was used to define the orientation of the tibia plateau. To calculate this angle, the angles between z-axes of the tibia plateau plane were used. Furthermore, the intraclass correlation coefficient (ICC) and 95% confidence interval (CI) were calculated for all angles for both intra- and interobserver measurements. This was done with the model: two-way random absolute agreement and a confidence interval of 95%.

Moreover, the intra-observer variability of manual detection was calculated for ten measurements using the Euclidian distances. Additionally, manual and software derived landmarks were compared by calculating Euclidian distances between corresponding landmarks. Lastly, the corresponding landmarks of one set of manual and semi-automatic landmarks were projected on a lower limb. This resulted in each landmark being shown twice on a single limb. These landmarks were visually compared and a score of one was given to the point which was located most accurately.

Euclidian distances were calculated using Excel (Microsoft Corporation, Microsoft Excel). ICC was computed using SPSS (IBM SPSS statistics, Chicago, USA).

5.1.8 Exclusion criteria

When the algorithm was not able to locate all landmarks, the set of measurements were excluded. Therefore, exclusion criteria were drafted. Measurements were excluded if visual analysis showed clear user errors. To evaluate whether the error was user related, the algorithm was applied again three times. When the algorithm could locate the landmarks correctly in all instances, the measurements were excluded. However, when errors were still present, the measurements were included as it was a shortcoming of the algorithm. Furthermore, when users manually selected landmarks, the measurements were excluded, as it results in validation of manual landmark selection.

5.2 METHOD VIRTUAL OSTEOTOMY

5.2.1 Study population

The second phase of this project entails the creation of virtual osteotomies. This phase included twenty femora and twenty tibiae from the same study population as used in the deformity analysis part. For both the femur and tibia, ten left and right limbs were included.

5.2.2 Methods

The segmentations of the lower limbs used in the deformity analysis script were used again for the virtual osteotomy. Using the deformity analysis algorithm, all landmarks, and angles of both the femur and tibia were found.

5.2.3 Requirements virtual osteotomy algorithm

The algorithms must fulfil several requirements, namely:

- Must work for both the left and right side of the lower limb.

- Capable of performing uniplanar and biplanar tibial osteotomies.
- Capable of performing an HTO and/or a DFO.
- If novel studies lead to new insights, the algorithm must be able to be adapted on these new insights.
- Contain a review process which compares the virtually achieved geometry to the proposed geometry.
- The algorithm should optimize the correction until the new geometry is within 0.1° of the proposed geometry. The cut-off value of 0.1°, which corresponds to 0.1 mm, was based on the UMCU SLS-printing precision of 0.1 mm. Therefore, the virtual osteotomy needs a maximum inaccuracy of 0.1°. Furthermore, increasing the accuracy results in a longer runtime of the algorithm. Whereas the goal is to keep the algorithm fast.

5.2.4 Distal femoral osteotomy algorithm

User input

First, the landmarks and angles of the femur, as noted in *Table 1* and *2,* are located and measured. Next, the user is asked if the virtual osteotomy must be performed on the left or right femur. After this, a pop-up box is shown in which the user must indicate the desired geometry of the femur after the osteotomy. The algorithm then calculates the needed correction wedge angles. In the case of valgisation osteotomy, the user is asked if a lateral opening wedge DFO or a medial closing wedge DFO should be performed. The next step is defining the cutting plane.

Cutting plane and hinge

First the entrance point of the osteotomy must be defined. For this a plane is constructed which runs through both the medial and lateral epicondyle. This plane is perpendicular to the coronal plane. Next, the plane is translated 25 mm proximally in the direction of the mechanical axis of the femur. This entrance height is in accordance with expert opinion of the orthopaedic surgeons at the UMCU. In case of a lateral opening or closing osteotomy, the entrance is located on the most lateral point of the femur in this plane. In a medial closing osteotomy, the point is located most medial. The user is then asked to globally indicate the location of the hinge. In medial closing wedge osteotomies, this point is located just above the lateral femoral condyle. The study of Kim *et al*. has shown that a hinge 15 mm above the upper border of the lateral condyle resulted in more hinge fractures as compared to a hinge on the upper border.[55] A plane parallel to the transversal plane is constructed with the hinge point as the origin. In this plane, the hinge is located. When a lateral osteotomy is performed, the hinge is the most medial part of the femur in this plane. In a medial osteotomy, the hinge is located lateral. The cutting plane runs through two points, the entrance of the saw cut and the osteotomy hinge. This plane is perpendicular to the coronal plane. After the cutting plane is constructed, the femur is cut in a proximal and distal part. All three planes can be seen in *Figure 11*.

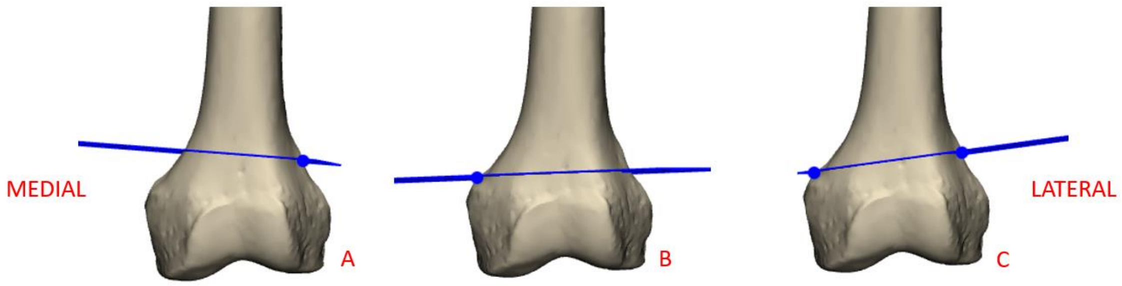

Figure 17: A) Shows the plane which is used to find the entrance point of the osteotomy. B) The plane that defines the location of the hinge. C) The cutting plane which runs through the entrance and hinge and is perpendicular to the coronal plane.

Rotation correction
After the femur is cut, rotational correction can be performed. The correction angle calculated earlier is used to perform the derotation. The axis of rotation is the mechanical axis. The axis itself is located at the hinge point. After a first derotation of the distal femur, the new femoral rotation is calculated. To find the new femoral rotation, the medial and lateral posterior condyle points are recalculated with the same method as used in the deformity analysis algorithm. This new femoral rotation is then compared to the desired femoral rotation. The difference between these angles is then calculated. If the difference is smaller than 0.1°, the algorithm advances to the next section. If the difference is larger than 0.1°, the distal femur is derotated again with the calculated difference. This process is repeated until the difference between desired and achieved femoral rotation is less than 0.1°. All rotations are added up to calculate the final performed correction.

Varisation or valgisation osteotomy
Derotation is followed by varisation or valgisation of the femur. Again, the correction angle is calculated by subtracting the current mLDFA from the desired mLDFA. The axis of rotation is a line perpendicular to the coronal plane. The line is located at the hinge. Around this axis, the distal femur and the lateral and medial epicondyle are rotated. After rotation, the distal points of the femur are remeasured. Using these new distal points, the new mLDFA is calculated. This new mLDFA is calculated in the new coronal plane which is formed after varisation or valgisation. As with derotation, the new mLDFA is compared to the desired mLDFA. When the difference is more than 0.1°, fine-tuning is performed with the same method as described in the derotation part. When the difference is less than 0.1°, the algorithm recalculates the femoral rotation and the LPFA. Also, the total mLDFA correction angle is calculated. Finally, the differences between all corrected angles and the desired angles are displayed.

Closed wedge osteotomy
In case of a closing wedge osteotomy, another cut must be made. By virtually rotating the femur, the distal and proximal part of the femur overlap. The earlier defined cutting plane is used to cut out the overlapping part of the proximal femur.

5.2.5 High tibial osteotomy algorithm

User input
Large parts of the algorithm for the HTO are comparable to the DFO algorithm. For the virtual HTO, the user is asked to input the desired four angles of the tibia, namely the MPTA, PPTA, rotation and LDTA. In case of a valgisation, the user is asked if a medial opening wedge (MOW) or lateral closing wedge (LCW) HTO should be performed. If a MOW HTO is chosen, a pop-up box appears in which the user must indicate if a biplanar osteotomy should be performed. A biplanar osteotomy is not possible when a valgisation and a decrease of tibial rotation are combined. As a result, the option of a biplanar osteotomy will not be available.

Cutting plane and hinge
The cutting plane for the HTO is constructed using three points. The first point is the entrance of the sawcut. This point is located most medial in the MOW and MCW HTO. For the LCW HTO, the entrance point is located most lateral. To define the entrance, the user indicates a point on the tibia. A plane parallel to the transversal plane is constructed based on this point. The most medial or lateral point of the tibia in this plane is the entrance of the sawcut. The second point is the hinge point. This point is located at the same height as the tip of the fibula. Again, a plane parallel to the transversal plane is constructed. The most lateral point in this plane is the hinge in case of an MCW or MOW HTO. The most medial point is the hinge in an LCW HTO. The last point is found by translating the sagittal tangent of the tibial plateau to the entrance point. The endpoint of this line is the third point used for the cutting plane. Using this endpoint ensures that the osteotomy is sawn in parallel to the tibial plateau. This is done to make sure that no slope correction is induced when varisation or valgisation is

performed.[56] With this plane, the tibia is cut in a proximal and distal tibia. *Figure 18* shows the two planes used to find the entrance and hinge. Furthermore, the cutting plane and translated sagittal tangent are displayed.

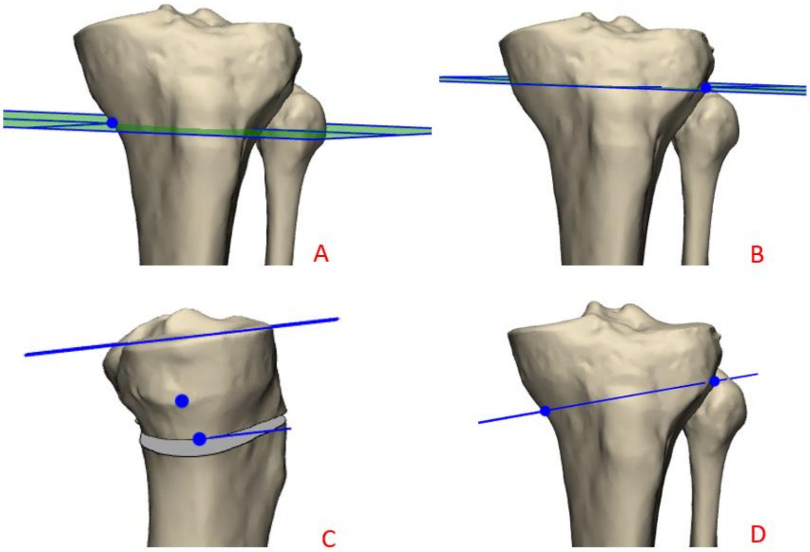

Figure 18: A) The plane used to find the entrance point. B) The plane used to find the hinge. C) The translated sagittal tangent, which is parallel to the proximal tibia plateau. D) The cutting plane which is based on the hinge, entrance, and sagittal tangent. The plane enters the tibia parallel to the tibial plateau.

Biplanar osteotomy

In case of a MOW HTO a biplanar osteotomy can be performed. In the case of a proximal biplanar the user must indicate a point just proximal of the tuberosity. A plane through this point and parallel to the coronal plane is constructed. This plane is then rotated so that it makes an angle of approximately 110° with respect to the transversal plane.[57] The biplanar plane is used to cut the tuberosity of the proximal tibia. After performing the cut, the tuberosity is merged with the distal tibia. An advantage of a biplanar osteotomy is that the smaller gap volume and wider bone contact is expected to result in faster bone formation. [58] Furthermore it increases rotational stability.[59]

Fibula

When an LCW HTO is performed, the fibula must be cut. This cut is made at 2/3 of the length of the fibula, from the tip of fibula down to the most distal part of the fibula.[60]

Derotation

First, derotation of the tibia can be performed. The axis of rotation is the mechanical axis of the tibia. This axis is relocated to the hinge point. In the same manner as in the DFO, fine-tuning is conducted to match the achieved and desired correction to within 0.1°. The distal tibia, tibial ankle centre, lateral and medial malleolus, distal tangent, and anatomical axis are rotated along.

Varisation or valgisation

After derotation of the tibia, varisation or valgisation is performed. The axis of rotation is the line perpendicular to the coronal plane. The axis runs through the hinge point which is found earlier by the algorithm. Fine-tuning of the correction is performed as mentioned earlier.

Slope correction

For a slope correction, the axis of rotation is parallel to the coronal tangent of the tibial plateau. This axis is then relocated to the hinge. When the desired slope is achieved, the algorithm advances to the last part.

Derotation optimisation
After the first derotation, varisation/valgisation, and slope correction, the tibial rotation is measured again. Due to the varisation, valgisation or slope correction, the tibial rotation can be changed, and therefore derotation must be optimised again. Derotation is performed as described under the heading *derotation*.

When the optimal tibial rotation is achieved, the other angles are calculated again. The differences between the desired and achieved angles are displayed. Also, the individual corrections are added to show total rotation, MPTA and PPTA correction.

5.2.6 Statistical analysis

For statistical analysis of the DFO algorithm, ten femora with a mLDFA smaller than or around 85° were selected to undergo LOW or MCW DFO. The virtual osteotomy was performed with a desired mLDFA 5° higher than the original mLDFA. This was combined with a derotation of the femur of 5°. Furthermore, a virtual osteotomy to achieve a desired mLDFA of 10° higher than original was performed. This correction was combined with a rotation of 10°. An overview is given in *Table 5*.

Table 5: Validation of the LOW DFO and MCW DFO. Desired angles and number of performed osteotomies are shown.

NO. OF OSTEOTOMIES	AVERAGE ORIGINAL MLDFA (°)	AVERAGE DESIRED MLDFA (°)	AVERAGE ORIGINAL ROTATION (°)	AVERAGE DESIRED ROTATION (°)
10X	Original mLDFA	Original mLDFA + 5°	Original rotation	Original rotation +/- 5°
10X	Original mLDFA	Original mLDFA + 10°	Original rotation	Original rotation +/- 10°

For the LCW DFO, ten femora with a mLDFA larger than or around 90° were selected. Here the same corrections are applied. *Table 6* shows an overview of performed osteotomies. In total, sixty virtual osteotomies were performed.

Table 6: Validation of the LCW DFO. Desired angles and number of performed osteotomies are shown.

NO. OF OSTEOTOMIES	AVERAGE ORIGINAL MLDFA (°)	AVERAGE DESIRED MLDFA (°)	AVERAGE ORIGINAL ROTATION (°)	AVERAGE DESIRED ROTATION (°)
10X	Original mLDFA	Original mLDFA - 5°	Original rotation	Original rotation +/- 5°
10X	Original mLDFA	Original mLDFA - 10°	Original rotation	Original rotation +/- 10°

Statistical analysis for the HTO algorithm is performed with the same approach as for the DFO algorithm. 10 Tibiae with a MPTA smaller than or around 85° are collected for virtual MOW and LCW HTO. Valgisation of 7° was performed in combination with a slope correction or rotation correction of 10°. *Table 7* shows the combinations of the virtual osteotomies.

Table 7: Validation of the MOW HTO and LCW HTO. Desired angles and number of performed osteotomies are shown.

NO. OF OSTEOTOMIES	AVERAGE ORIGINAL MPTA (°)	AVERAGE DESIRED MPTA (°)	AVERAGE DESIRED ROTATION (°)	AVERAGE DESIRED PPTA (°)
10X	Original MPTA	Original MPTA + 7°	Original rotation	Original PPTA +/- 10°
10X	Original MPTA	Original MPTA + 7°	Original rotation +/- 10°	Original PPTA

Furthermore, ten tibiae with a MPTA larger or around 90° were selected for virtual MCW HTO. Here, a varisation of 5° and 10° was performed. Again, this was in combination with a 10° slope or rotation correction. This resulted in a total of sixty virtual osteotomies.

Table 8: Validation of the MCW HTO. Desired angles and number of performed osteotomies are shown

NO. OF OSTEOTOMIES	AVERAGE ORIGINAL MPTA (°)	AVERAGE DESIRED MPTA (°)	AVERAGE DESIRED ROTATION (°)	AVERAGE DESIRED PPTA (°)
10X	Original MPTA	Original MPTA - 7°	Original rotation	Original PPTA +/- 10°
10X	Original MPTA	Original MPTA - 7°	Original rotation +/- 10°	Original PPTA

For all corrections, the difference between the achieved and desired angle is calculated. Furthermore, for each technique, the ten measurements are combined to find a mean difference and the standard deviation. Also, the mean and standard deviation of the performed correction are calculated.

5.3 METHOD PERSONALIZED SURGICAL INSTRUMENT

5.3.1 Requirements PSI algorithm

After virtual osteotomy planning, the PSI is developed. This process is captured in a semi-automatic algorithm. After the design of the PSI, it is printed using an inhouse SLS-printer. Therefore, the PSI must take various requirements into account:

- The PSI should be 3D printable. Therefore, it needs a minimum thickness of 0.7 mm and does not contain details smaller than 1.5 mm.[62,63]
- The PSI base must match with the surface of the underlying bone, either the tibia or the femur.
- The drill guides of the PSI must pair with the location of the screws. In total, the PSI should contain, depending on the plate, three to eight drill guides with a diameter of 4 mm. The drill guides should be at least 10 mm deep. The minimal inner diameter of the holes should be 4.2 ± 0.1 mm, so the drill does not make contact with the PSI. Moreover, the drill holes should give maximal support to the stainless-steel inserts. The outer diameter of the holes should be 6.0 ± 0.1 mm.
- Take the thickness and width of the saw blade into account. The thickness of the sawblade is 1.2 mm. The width of the sawblade is 27 mm. Therefore, the saw guide must at least have a dimension of 1.4x29 mm.
- Contain three holes for the k-wire inserts. The k-wires hold the PSI in place during surgery. The holes should be at least 10 mm deep. The diameter should be 3.5 ± 0.1 mm.[64] In the bottom 5 mm, the inner diameter of the holes for the k-wires should have a diameter of 2.25 ± 0.1 mm.
- The PSI must be easy to place during surgery; therefore, a trade-off is made between smallest possible size and largest possible surface for an optimal fit.

- The PSI cannot have any sharp edges, as these edges could injure tissue surrounding the knee joint during surgery.

Besides the requirements to the PSI, the algorithm that is used to develop the PSI has several prerequisites:
- Must work for both left and right lower limb.
- Both the design of a PSI for an HTO and/or DFO must be possible.
- Should contain several check points where the user can adjust the PSI if necessary.

5.3.2 PSI algorithm

After performing the virtual osteotomy, the PSI can be designed. First, the user must load and place the osteotomy plate. The osteotomy plate includes cylinders, which resemble the screws. These cylinders fit in the screw holes.

Inverse osteotomy
After placement of the plate, the distal femur or tibia and the cylinders are rotated inversely to the virtual osteotomy. In this way, the femur resembles the pre-operative state.

PSI base
Next, the user must manually select several points on which a curve is based. This curve is used to design the base of the PSI. The surface of this base is then given an offset of 15 mm. For the DFO algorithm, the offset is given into the sagittal direction. For the HTO algorithm, a plane is fitted to the surface of the base. The offset is then given perpendicular to this plane. The contour of the base is found and given a fillet with a radius of 2 mm.

Screw guides
The cylinders for the screw holes, with a diameter of 4.2 mm are then subtracted from this base. Next, a diameter of 6 mm is assigned to the cylinders. The cylinders are then translated, so they are in the upper 10 mm of the base. Again, the cylinders are subtracted, which leaves room for the stainless-steel inserts.

Sawguide
The following step is to design the sawguide. The sawguide is designed in such a way, that when the oscillating saw is inserted fully, it just reaches the hinge. Therefore, the distance of the hinge to the entrance of the sawguide is 69 mm maximal. The width of the inlet is 1.4 mm. The length of the inlet is equal to the width in the AP-direction of the bone. 6.7 mm is added because of the oscillation of the saw. In case of an opening wedge osteotomy, this inlet is wrapped. The sawguide is then cut 10 mm inward from the osteotomy entrance. In case of a closing wedge osteotomy, two inlets are needed. Around these inlets, a box is created, which is then wrapped. This results in smooth edges of the box.

K-wires
Next, holes for the three k-wire inserts are designed. The first two k-wires are located close to the sawplane and run perpendicular to this plane. The algorithm places these two k-wires anterior and posterior to the sawguide. In case of a DFO the hinge protecting k-wire is located next to the second most proximal screw. When an HTO is performed, the k-wire is located near the most distal screw. The algorithm evaluates whether this k-wire intersects with one of the screws. Again, cylinders with a diameter of 2.2 mm are subtracted from the base. Duplicates of these cylinders with a diameter of 3.5 mm are subtracted from the upper 10 mm of the base, to make space for the inserts. If the PSI is not able to give enough support, an additional guide is constructed with an outer diameter of 4.5 mm.

Winglets
Besides the winglets from the sawguide, two additional winglets are constructed. These winglets are located at the same height as the hinge protecting k-wire. The winglets have a width of 10 mm and a thickness of 3 mm. The edges are rounded using a fillet with a radius of 2 mm.

5.3.3 PSI analysis
For analysis of the PSI algorithm, six PSI's were designed for the femur and four for the tibia. Several measurements were taken using the measurement software available in 3-matic. The diameters of the drill guides and k-wire guides were measured and compared to the design criteria. Furthermore, the width and length of the sawguide were measured. The direction of the screws and k-wires were visually inspected.

6 RESULTS

6.1 RESULTS 3D-DEFORMITY ANALYSIS

In this study, forty lower limbs of patients who underwent a lower limb CT-scan were analysed. In *Figure 19* an example of the result of a segmentation in Mimics is shown. The femora and tibiae of this patient were segmented. The bones were wrapped and smoothed, however, minor imperfections were still present.

Figure 19: Front and back view of the segmentation of the lower limbs.

6.1.1 Deformity analysis of the femur

Intra-observer variability ranged from 0.0 ± 0.2 mm for the FLCD to 2.1 ± 3.3 mm for the FCM. The epicondyle points showed the largest variability. Interobserver variability ranged between 0.1 ± 0.8 mm for the FLCD to 5.3 ± 5.2 mm for the FCM. Again, the mean Euclidian distance was largest for the landmarks related to the epicondyles. All mean Euclidian distances are stated in *Table 9, Figure 20* and *21.*

Table 9: Euclidian distance of all bony landmarks of both the left and right femur for the intra-observer variability.

BONY LANDMARK	INTRA-OBSERVER EUCLIDEAN DISTANCE, MM (MEAN ± SD)	INTEROBSERVER EUCLIDEAN DISTANCE, MM (MEAN ± SD)
FEMORAL HIP CENTRE (FHC)	0.2 ± 0.3	0.3 ± 0.3
FEMORAL NECK CENTRE (FNC)	0.3 ± 0.4	0.3 ± 0.4
LATERAL EPICONDYLE (FCL)	0.8 ± 1.4	1.9 ± 2.4
MEDIAL EPICONDYLE (FCM)	2.1 ± 3.3	5.3 ± 5.1
TRANSEPICONDYLAR MIDPOINT (TEM)	1.2 ± 1.5	2.4 ± 2.2
FEMORAL NOTCH POINT (FNP)	1.0 ± 1.1	0.8 ± 0.9
TIP OF GREATER TROCHANTER (TGT)	0.1 ± 0.9	0.4 ± 1.8
FEMORAL LATERAL CONDYLE POSTERIOR (FLCP)	0.4 ± 1.1	1.1 ± 2.0
FEMORAL MEDIAL CONDYLE POSTERIOR (FMCP)	0.4 ± 1.3	1.2 ± 2.0
FEMORAL LATERAL CONDYLE DISTAL (FLCD)	0.0 ± 0.2	0.1 ± 0.8
FEMORAL MEDIAL CONDYLE DISTAL (FMCD)	0.4 ± 1.6	0.3 ± 1.3

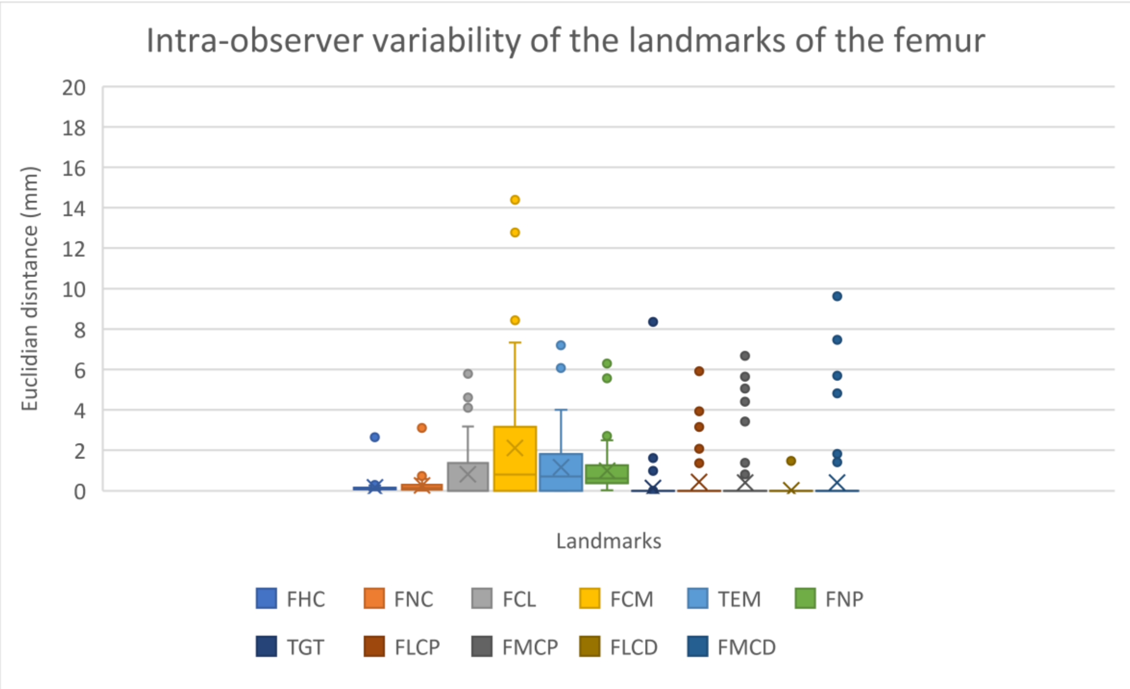

Figure 20: Boxplot of the intra-observer variability for all landmarks of the femur.

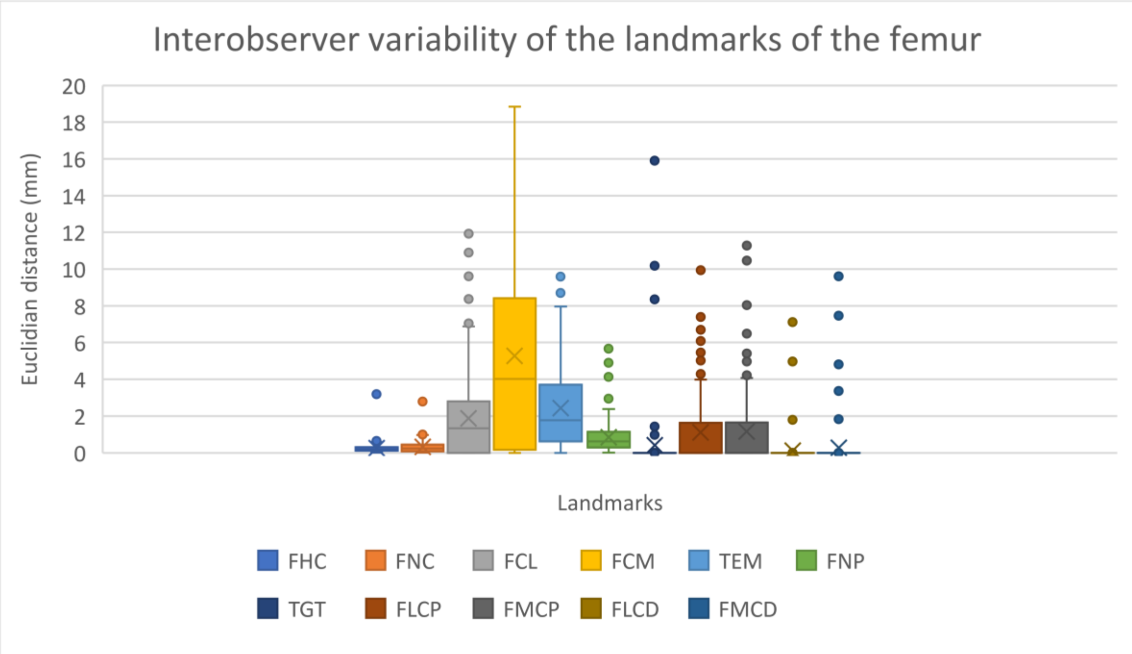

Figure 21: Boxplot of the interobserver variability for all landmarks of the femur.

Table 10 shows the intra- and interobserver agreement for the measured angles of the femur. The mean intra-observer difference ranged between 0.1° ± 0.1° and 0.2° ± 0.2°. The mean interobserver difference ranged between 0.1° ± 0.1° and 0.3° ± 0.5°.

Table 10: Intra-observer agreement for the angles of the left and right femur

ANGLE	INTRA-OBSERVER, DEGREES (MEAN ± SD)	INTEROBSERVER, DEGREES (MEAN ± SD)
LPFA	0.2 ± 0.4	0.3 ± 0.5
MLDFA	0.1 ± 0.1	0.1 ± 0.1
FEMORAL ROTATION	0.2 ± 0.2	0.3 ± 0.2

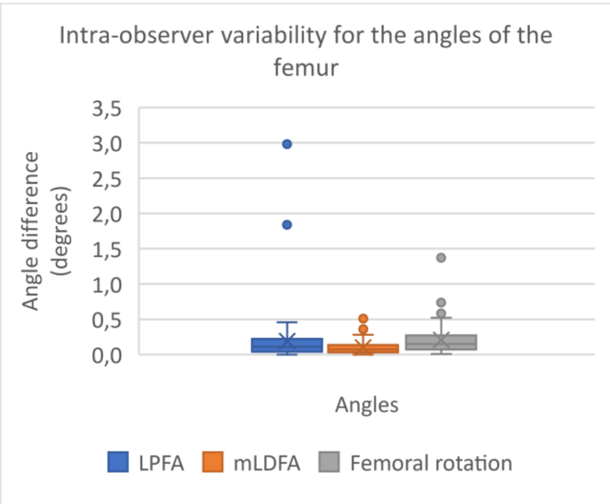

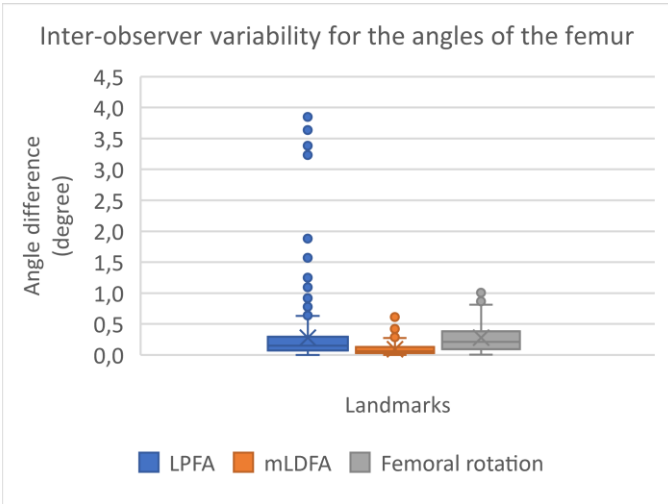

Figure 22: Boxplots of the intra- and interobserver agreement for the angles of the femur.

Furthermore, ICCs were calculated for the angles of the femur. Perfect agreement for both intra- and interobserver measurements was achieved for all angles, as can be seen in *Table 11*.

Table 11: Intraclass correlation coefficient (ICC) for the angles of the femur for the intra-observer and interobserver measurements

ANGLE	ICC INTRA-OBSERVER	95% CI INTRA-OBSERVER	ICC INTEROBSERVER	95% CI INTEROBSERVER
LPFA	1.00	0.99 < ICC < 1.00	0.99	0.99 < ICC < 1.00
MLDFA	1.00	1.00 < ICC < 1.00	1.00	1.00 < ICC < 1.00
FEMORAL ROTATION	1.00	1.00 < ICC < 1.00	1.00	1.00 < ICC < 1.00

6.1.2 Deformity analysis of the tibia

Intra-observer variability ranged between 0.0 ± 0.1 mm for the tibiofibular point to 3.1 ± 2.9 mm for the medial tuberosity. The interobserver agreement was calculated using 231 measurements. Three sets of measurements (nine in total) were excluded due to several reasons. In one instance, one observer was not able to complete the entire deformity analysis process, due to the algorithm missing landmarks. The two other sets were excluded because of erroneous user input resulting in a faulty landmark location. This was decided after visual inspection and applying the algorithm again. Furthermore, five sets of the TLCP and tibial rotation were excluded, as users manually selected the TLCP. Interobserver agreement ranged between 0.1 ± 0.1 mm for the TAAP to 3.8 ± 4.0 mm for the medial tuberosity. In *Table 12*, the intra- and interobserver agreement for all landmarks are listed. *Figures 23* and 24 show boxplots of the Euclidian distances of the landmarks for the intra- and interobserver agreement. *Figures 23* and 24 display boxplots of all intra- and interobserver Euclidian distances.

Table 12: Euclidean distance of all bony landmarks of the left and right tibia

BONY LANDMARK	INTRA-OBSERVER EUCLIDEAN DISTANCE, MM (MEAN ± SD)	INTEROBSERVER EUCLIDEAN DISTANCE, MM (MEAN ± SD)
TIBIAL KNEE CENTRE (TKC)	0.4 ± 0.3	0.4 ± 1.3
TIBIAL ANKLE CENTRE (TAC)	1.2 ± 0.6	1.3 ± 0.7
TIBIAL MEDIAL INTERCONDYLAR TUBERCLE (TMIT)	0.3 ± 1.5	0.8 ± 2.6
TIBIAL LATERAL INTERCONDYLAR TUBERCLE (TLIT)	0.3 ± 1.7	0.8 ± 2.7
TIBIAL MEDIAL CONDYLE POSTERIOR (TMCP)	0.3 ± 0.4	0.4 ± 0.6
TIBIAL LATERAL CONDYLE POSTERIOR (TLCP)	0.5 ± 1.8	1.1 ± 3.1
TIBIAL ANATOMICAL AXIS PROXIMAL (TAAP)	0.1 ± 0.1	0.1 ± 0.1
TIBIAL ANATOMICAL AXIS DISTAL (TAAD)	0.1 ± 0.1	0.2 ± 0.1
TIBIAL MEDIAL MALLEOLUS (TMM)	1.1 ± 2.8	0.7 ± 1.5
FIBULAR LATERAL MALLEOLUS (FLM)	0.6 ± 0.5	0.9 ± 2.2
TIBIOFIBULAR POINT	0.0 ± 0.1	0.1 ± 0.3
PCL INSERTIA	1.3 ± 0.8	2.0 ± 1.1
MEDIAL TUBEROSITY	3.1 ± 2.9	3.8 ± 4.0

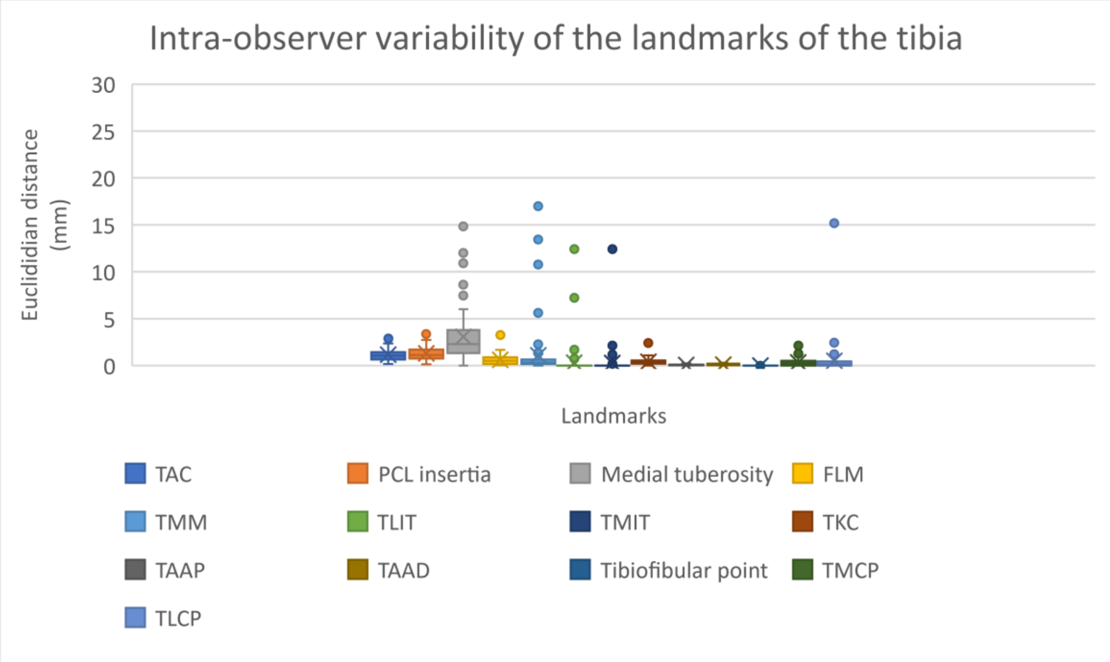

Figure 23: Boxplot of the intra-observer variability for all landmarks of the tibia.

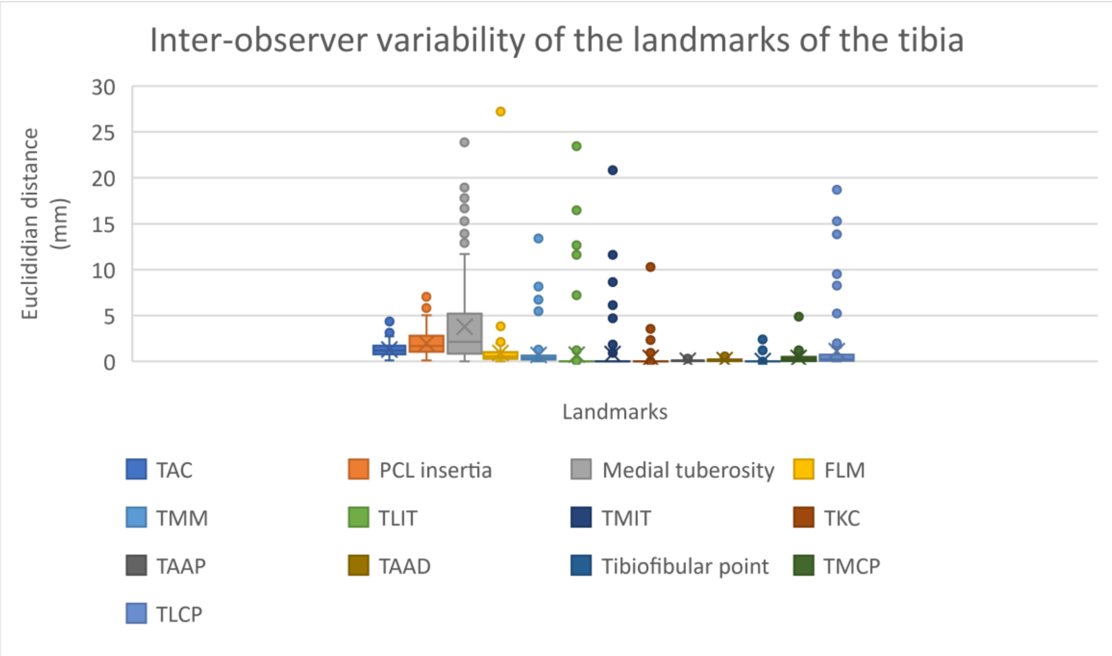

Figure 24: Boxplot of the interobserver variability for all landmarks of the tibia.

Mean intra-observer variability for the measured angles ranged between 0.2° ± 0.2° for MPTA to 1.0° ± 1.2° for the LDTA. Mean intra-observer variability for the direction of the tibia plateau was 0.6° ± 0.5°. Mean interobserver variability ranged between 0.3° ± 0.3° for the MPTA to 0.8° ± 0.8° for the LDTA. Tibia plateau orientation interobserver variability was 0.7° ± 0.5°. *Table 13* shows the intra- and interobserver variability. Boxplots of the measured angles are displayed in *Figure 25*.

Table 13: Intra observer agreement for the angles of the left and right tibia

	INTRA-OBSERVER, DEGREES (MEAN ± SD)	INTEROBSERVER, DEGREES (MEAN ± SD)
MPTA	0.2 ± 0.2	0.3 ± 0.3
LDTA	1.0 ± 1.2	0.8 ± 0.8
PPTA	0.5 ± 0.5	0.7 ± 0.6
TIBIAL ROTATION	0.5 ± 1.1	0.6 ± 1.3

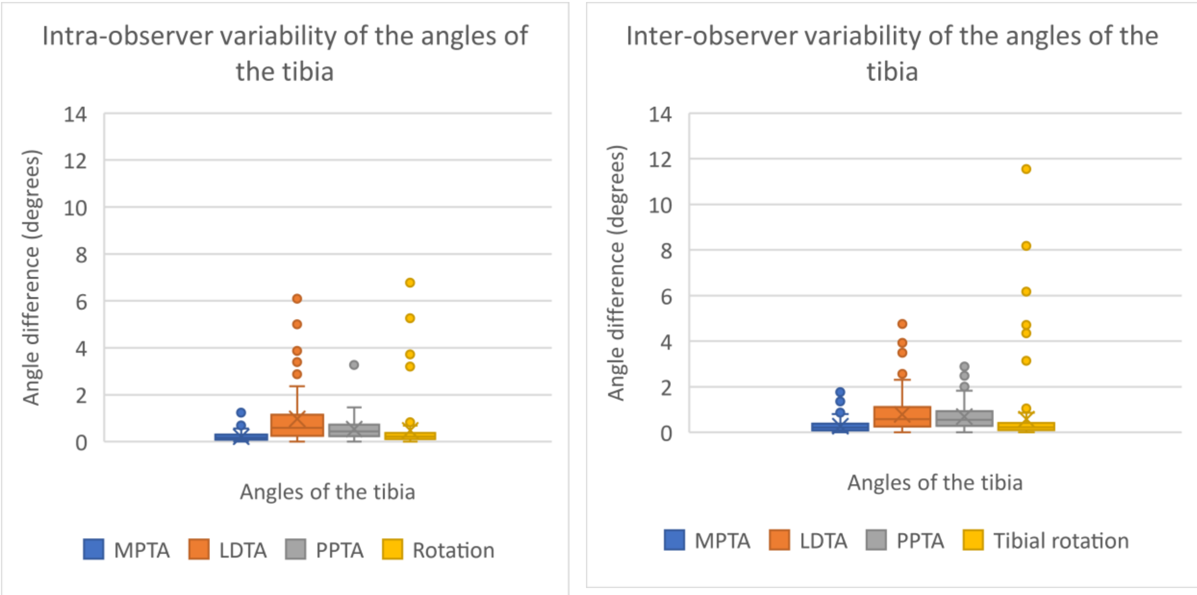

Figure 25: Boxplots of the intra- and interobserver agreement for the angles of the tibia.

Furthermore, ICC calculations for the intra-observer agreement for the angles of the femur showed good reliability for the LDTA and perfect agreement for the MPTA, PPTA and tibial rotation. The interobserver ICC was perfect for all angles as can be seen in *Table 14*.

Table 14: Intraclass correlation coefficient (ICC) for the angles of the tibia for the intra- and interobserver measurements

ANGLE	ICC INTRA-OBSERVER	95% CI INTRA-OBSERVER	ICC INTEROBSERVER	95% CI INTEROBSERVER
MPTA	0.99	0.98 < ICC 0.99	0.99	0.97 < ICC < 0.99
LDTA	0.89	0.83 < ICC < 0.93	0.93	0.89 < ICC < 0.95
PPTA	0.97	0.95 < ICC < 0.98	0.96	0.95 < ICC < 0.98
TIBIAL ROTATION	0.99	0.98 < ICC < 0.99	0.98	0.97 < ICC < 0.99

6.1.3 Manual landmark detection intra-observer variability

Table 15 and *16* show the mean Euclidian distances of the manually annotated femoral and tibial landmarks. Intra-observer agreement of the manual process was lower for all landmarks when compared to the algorithm. *Figures 26* and *27* show the boxplots for the femoral and tibial landmarks.

Table 15: Intra-observer variability of the manual detection of the femoral landmarks

BONY LANDMARK	MANUAL MEASUREMENT, EUCLIDEAN DISTANCE, MM (MEAN ± SD)	SEMI-AUTOMATIC MEASUREMENT, EUCLIDEAN DISTANCE, MM (MEAN ± SD)
FEMORAL HIP CENTRE (FHC)	3.8 ± 1.6	0.2 ± 0.3
FEMORAL NECK CENTRE (FNC)	5.7 ± 6.3	0.3 ± 0.4
LATERAL EPICONDYLE (FCL)	2.8 ± 3.1	0.8 ± 1.4
MEDIAL EPICONDYLE (FCM)	4.0 ± 3.1	2.1 ± 3.3
TRANSEPICONDYLAR MIDPOINT (TEM)	3.0 ± 2.6	1.2 ± 1.5
FEMORAL NOTCH POINT (FNP)	3.2 ± 2.1	1.0 ± 1.1
TIP OF GREATER TROCHANTER (TGT)	6.3 ± 4.9	0.1 ± 1.0
FEMORAL LATERAL CONDYLE POSTERIOR (FLCP)	3.2 ± 1.4	0.4 ± 1.1
FEMORAL MEDIAL CONDYLE POSTERIOR (FMCP)	3.7 ± 1.2	0.4 ± 1.3
FEMORAL LATERAL CONDYLE DISTAL (FLCD)	8.0 ± 5.6	0.0 ± 0.2
FEMORAL MEDIAL CONDYLE DISTAL (FMCD)	7.6 ± 5.7	0.4 ± 1.6

Table 16: Intra-observer variability for the manual selection of the tibial landmarks

BONY LANDMARK	MANUAL MEASUREMENT, EUCLIDEAN DISTANCE, MM (MEAN ± SD)	SEMI-AUTOMATIC MEASUREMENT, EUCLIDEAN DISTANCE, MM (MEAN ± SD)
TIBIAL KNEE CENTRE (TKC)	1.8 ± 1.6	0.4 ± 0.3
TIBIAL ANKLE CENTRE (TAC)	1.2 ± 0.7	1.2 ± 0.6
TIBIAL MEDIAL INTERCONDYLAR TUBERCLE (TMIT)	1.1 ± 0.4	0.3 ± 1.5
TIBIAL LATERAL INTERCONDYLAR TUBERCLE (TLIT)	1.4 ± 1.0	0.3 ± 1.7
TIBIAL MEDIAL CONDYLE POSTERIOR (TMCP)	2.9 ± 2.0	0.3 ± 0.4
TIBIAL LATERAL CONDYLE POSTERIOR (TLCP)	3.1 ± 3.6	0.5 ± 1.8
TIBIAL ANATOMICAL AXIS PROXIMAL (TAAP)	1.2 ± 0.4	0.1 ± 0.0
TIBIAL ANATOMICAL AXIS DISTAL (TAAD)	0.9 ± 0.0	0.1 ± 0.1
TIBIAL MEDIAL MALLEOLUS (TMM)	1.0 ± 0.6	1.1 ± 2.8
FIBULAR LATERAL MALLEOLUS (FLM)	0.6 ± 0.3	0.6 ± 0.5
TIBIOFIBULAR POINT	1.4 ± 1.0	0.0 ± 0.1
PCL INSERTIA	1.4 ± 0.9	1.3 ± 0.8
MEDIAL TUBEROSITY	4.2 ± 3.4	3.1 ± 2.9

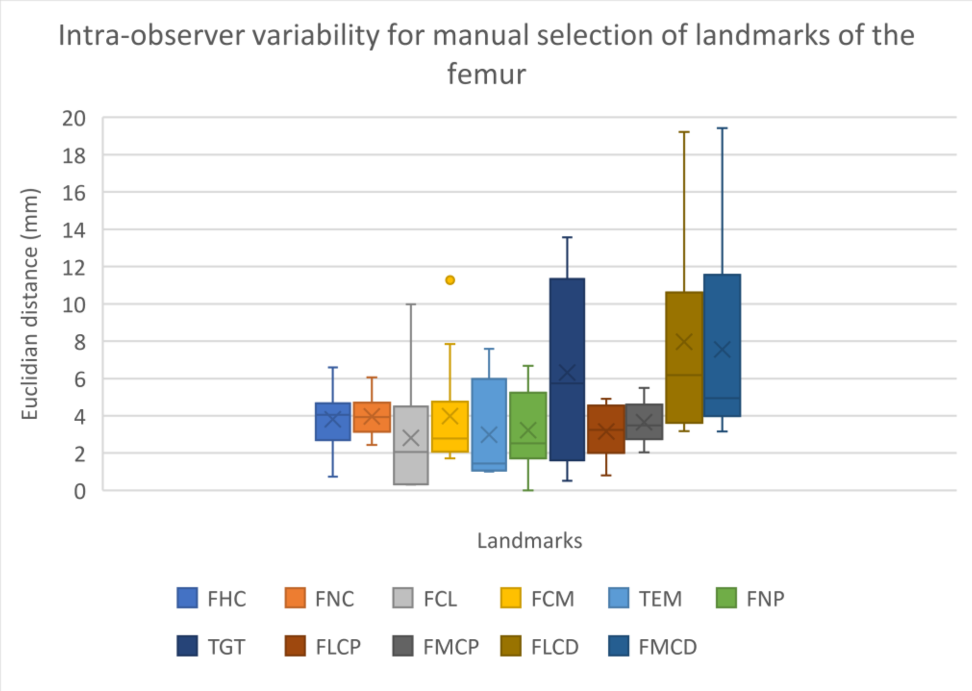

Figure 26: Intra-observer variability for manual selection of landmarks of the femur

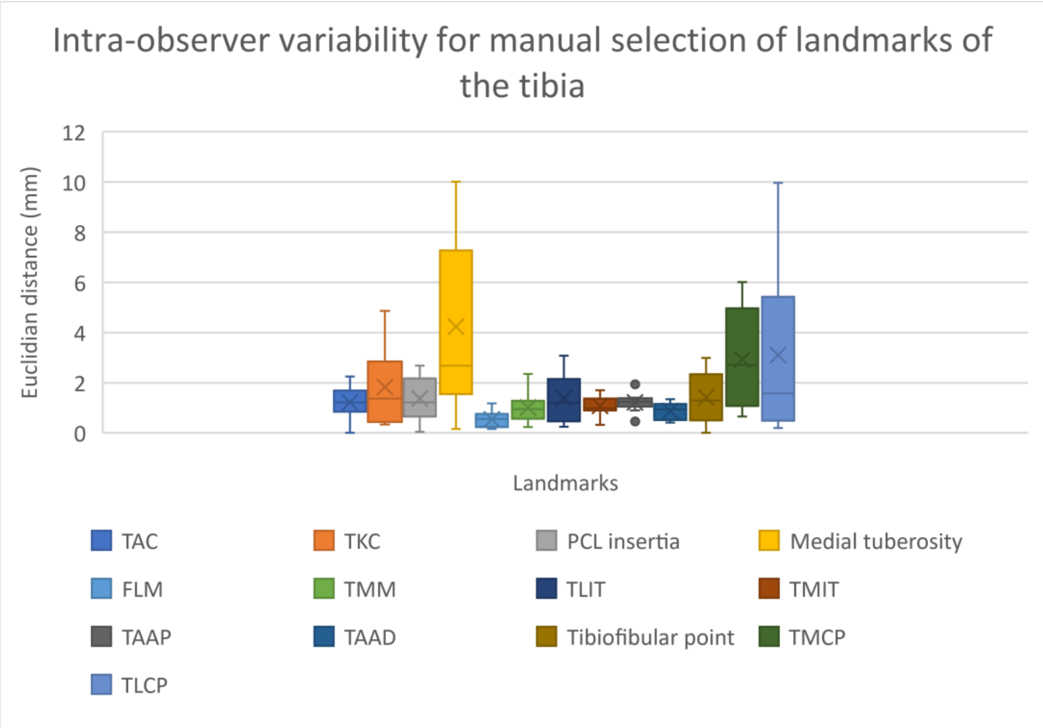

Figure 27: Intra-observer variability for manual selection of landmarks of the tibia.

6.1.4 Manual versus semi-automatic landmark detection

The Euclidian distances between the manually and software derived landmarks were calculated. As listed in *Table 17* and *18*, these distances were comparable to the manual intra-observer measurements. Visual inspection of manually versus software derived landmarks resulted in the scores as displayed in *Table 19*. This showed that the algorithm has a better accuracy than manual annotation.

Table 17: Mean Euclidean distance between manual selection of landmarks versus semi-automatic detection with the algorithm

BONY LANDMARK	EUCLIDEAN DISTANCE, MM (MEAN ± SD)
FEMORAL HIP CENTRE (FHC)	3.8 ± 1.6
FEMORAL NECK CENTRE (FNC)	5.7 ± 6.3
LATERAL EPICONDYLE (FCL)	2.8 ± 3.1
MEDIAL EPICONDYLE (FCM)	4.0 ± 3.1
TRANSEPICONDYLAR MIDPOINT (TEM)	3.0 ± 2.6
FEMORAL NOTCH POINT (FNP)	3.2 ± 2.1
TIP OF GREATER TROCHANTER (TGT)	6.3 ± 4.9
FEMORAL LATERAL CONDYLE POSTERIOR (FLCP)	3.2 ± 1.4
FEMORAL MEDIAL CONDYLE POSTERIOR (FMCP)	3.7 ± 1.2
FEMORAL LATERAL CONDYLE DISTAL (FLCD)	8.0 ± 5.6
FEMORAL MEDIAL CONDYLE DISTAL (FMCD)	7.6 ± 5.7

Table 18: Mean Euclidean distance between manual selection of landmarks versus semi-automatic detection with the algorithm

BONY LANDMARK	EUCLIDEAN DISTANCE, MM (MEAN ± SD)
TIBIAL KNEE CENTRE (TKC)	6.8 ± 4.3
TIBIAL ANKLE CENTRE (TAC)	1.5 ± 0.5
TIBIAL MEDIAL INTERCONDYLAR TUBERCLE (TMIT)	2.5 ± 1.0
TIBIAL LATERAL INTERCONDYLAR TUBERCLE (TLIT)	1.0 ± 0.8
TIBIAL MEDIAL CONDYLE POSTERIOR (TMCP)	3.8 ± 3.8
TIBIAL LATERAL CONDYLE POSTERIOR (TLCP)	8.9 ± 8.8
TIBIAL ANATOMICAL AXIS PROXIMAL (TAAP)	0.9 ± 0.8
TIBIAL ANATOMICAL AXIS DISTAL (TAAD)	1.1 ± 0.4
TIBIAL MEDIAL MALLEOLUS (TMM)	2.7 ± 1.1
FIBULAR LATERAL MALLEOLUS (FLM)	3.5 ± 1.7
TIBIOFIBULAR POINT	2.0 ± 0.9
PCL INSERTIA	1.9 ± 0.7
MEDIAL TUBEROSITY	2.9 ± 1.3

Table 19: Scores for the algorithm versus manual landmark location as determined by visual inspection.

	FEMUR	TIBIA
ALGORITHM	41x	35x
MANUAL	3x	2x
NO CHOICE POSSIBLE	11x	28x

6.2 Results virtual osteotomy

After deformity analysis was completed, the virtual osteotomy was performed. In this part of the study, forty patients were included. In total, twenty femora and twenty tibiae were included.

6.2.1 Distal femoral osteotomy

6.2.1.1 LOW DFO

For validation of the virtual LOW DFO algorithm, ten femora were used. Mean mLDFA was 83.8° ± 0.9° and mean femoral version was 9.0° ± 5.8°. In total, twenty virtual osteotomies were performed. *Table*

20 shows the differences between the desired and achieved mLDFA and rotation correction. The mLDFA correction accuracy was within 0.12° and the rotation correction accuracy was within 0.55°. Mean mLDFA correction accuracy was 0.06° ± 0.05° and mean rotation correction accuracy was 0.15° ± 0.17°. Furthermore, the total performed correction is displayed. In *Figure* 28 a virtual DFO is shown. *Appendix A Figure 33* shows histograms of the difference between achieved and desired geometry.

Table 20: In the first column the desired new geometry can be seen. Next, the difference between the achieved geometry and desired geometry is displayed. The last column shows the amount of correction which has been performed to reach the achieved geometry.

mLDFA correction (°)	**Difference (°) (Mean ± SD)**	**Performed correction (°) (Mean ± SD)**
Original + 5.0	0.06 ± 0.06	5.29 ± 0.25
Original + 10.0	0.05 ± 0.05	10.86 ± 0.37

Rotation correction (°)	**Difference (°) (Mean ± SD)**	**Performed correction (°) (Mean ± SD)**
Original +/- 5.0	0.10 ± 0.11	4.64 ± 0.05
Original +/- 10.0	0.20 ± 0.23	9.29 ± 0.10

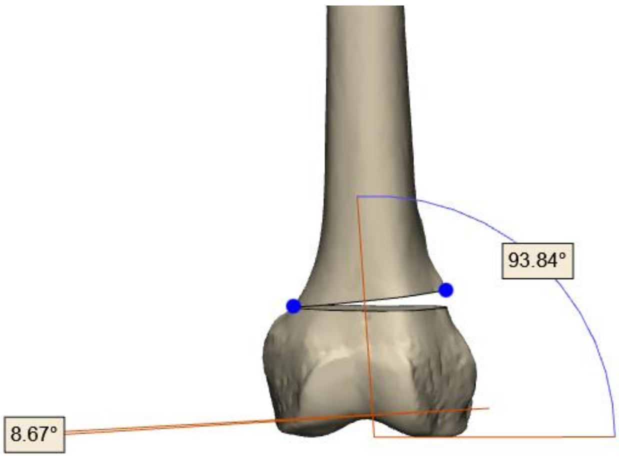

Figure 28: Virtual osteotomy of a femur. A 6.34° MPTA correction was performed.

6.2.1.2 MCW DFO

Validation of the virtual MCW DFO algorithm used the same ten femora as used in validation of the LOW DFO algorithm. Again, twenty virtual osteotomies were performed. In *Table 21* the differences between the desired and achieved mLDFA and rotation correction are displayed. The mLDFA correction accuracy was within 0.13° and the rotation correction accuracy was within 0.47°. Mean mLDFA correction accuracy was 0.04° ± 0.04° and mean rotation correction accuracy was 0.12° ± 0.17°. Histograms of the difference between achieved and desired geometry are displayed in *Appendix A Figure 34*.

Table 21: In the first column the desired new geometry can be seen. Next, the difference between the achieved geometry and desired geometry is displayed. The last column shows the amount of correction which has been performed to reach the achieved geometry.

mLDFA correction (°)	**Difference (°) (Mean ± SD)**	**Performed correction (°) (Mean ± SD)**
Original + 5.0	0.04 ± 0.04	5.32 ± 0.23
Original + 10.0	0.05 ± 0.06	10.88 ± 0.41

Rotation correction (°)	Difference (°) (Mean ± SD)	Performed correction (°) (Mean ± SD)
Original +/- 5.0	0.05 ± 0.06	5.35 ± 0.04
Original +/- 10.0	0.18 + 0.23	10.70 ± 0.07

6.2.1.3 LCW DFO

Virtual LCW DFO algorithm validation required ten different femora. Mean mLDFA was 89.1° ± 1.15° and mean rotation was 8.1° ± 5.4°. In total, eighteen virtual osteotomies were performed. Of these eighteen osteotomies, ten had a mLDFA correction of -5.0° and rotation correction of +/- 5.0°. Eight virtual osteotomies had a mLDFA correction of -10.0° and rotation correction of +/- 10.0°. Virtual correction of two femora resulted in error messages of the script and could therefore not be performed. The mLDFA correction accuracy was within 0.10° and the rotation correction accuracy was within 0.48°. Mean mLDFA correction accuracy was 0.03° ± 0.04° and mean rotation correction accuracy was 0.16° ± 0.13°. *Table 22* shows the final differences and performed corrections. Histograms of the difference between achieved and desired geometry are shown in *Appendix A Figure 35.*

Table 22: In the first column the desired new geometry can be seen. Next, the difference between the achieved geometry and desired geometry is displayed. The last column shows the amount of correction which has been performed to reach the achieved geometry.

mLDFA correction (°)	**Difference (°) (Mean ± SD)**	**Performed correction (°) (Mean ± SD)**
Original – 5.0	0.03 ± 0.02	-5.45 ± 0.15
Original – 10.0	0.03 ± 0.05	-10.59 ± 0.64

Rotation correction (°)	**Difference (°) (Mean ± SD)**	**Performed correction (°) (Mean ± SD)**
Original +/- 5.0	0.10 ± 0.10	4.70 ± 0.06
Original +/- 10.0	0.21 ± 0.11	9.45 ± 0.10

6.2.2 High tibial osteotomy

6.2.2.1 MOW HTO

Analysis of the MOW HTO algorithm required ten tibiae. These tibiae had a mean MPTA of 83.8° ± 1.2°, mean tibial rotation of 35.4° ± 8.7°, and a PPTA of 79.2 ± 2.5°. A MPTA correction of 7.0° in combination with a rotation or slope correction of +/- 10.0° was performed. The differences between achieved and desired correction are shown in *Table 23*. MPTA correction accuracy was within 0.09°, PPTA correction accuracy within 0.07° and rotation correction accuracy within 0.09°. Mean correction accuracies were: MPTA 0.03° ± 0.04°, PPTA 0.01° ± 0.03° and tibial rotation 0.02° ± 0.04°. *Table 28* shows the mean performed corrections. In *Figure 29* a biplanar osteotomy after a 5.0° MPTA correction can be seen. *Appendix A Figure 36* shows the histograms of the differences in achieved and desired geometry.

Table 23: The desired corrections in all three planes of the tibia and the average differences between the desired and achieved geometry.

MPTA correction (°)	**Difference (°) (Mean ± SD)**	**Rotation correction (°)**	**Difference (°) (Mean ± SD)**	**PPTA correction (°)**	**Difference (°) (Mean ± SD)**
Original + 7.0	0.03 ± 0.04	Original +/- 10.0	0.02 ± 0.04	Original +/- 10.0	0.01 ± 0.03

Table 24: Average performed correction of the MPTA, rotation and PPTA.

Performed MPTA correction (°) (Mean ± SD)	Performed rotation correction (°) (Mean ± SD)	Performed PPTA correction (°) (Mean ± SD)
7.37 + 0.14	10.01 + 0.14	9.02 + 2.07

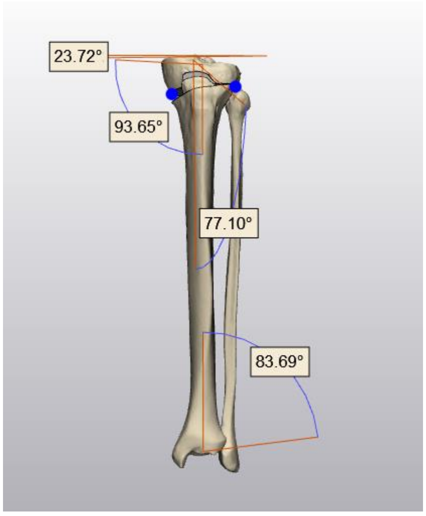

Figure 29: Virtual biplanar osteotomy of a tibia. A 5.0° MPTA correction was performed.

6.2.2.2 LCW HTO

LCW HTO algorithm validation used the same tibiae as MOW HTO validation. *Table 25 and 26* show the mean differences between desired\achieved geometry and performed correction. MPTA correction accuracy was within 0.06°, PPTA correction accuracy within 0.05°, and rotation correction accuracy within 0.08°. Mean correction accuracies were: MPTA 0.02° ± 0.03°, PPTA 0.01± 0.02°, and tibial rotation 0.00° ± 0.05°. *Appendix A Figure 37* shows the histograms of these differences.

Table 25: The desired corrections in all three planes of the tibia and the average differences between the desired and achieved geometry.

MPTA correction (°)	Difference (°) (Mean ± SD)	Rotation correction (°)	Difference (°) (Mean ± SD)	PPTA correction (°)	Difference (°) (Mean ± SD)
Original + 7.0	0.02 ± 0.03	Original +/- 10.0	0.00 ± 0.04	Original +/- 10.0	0.01 ± 0.02

Table 26: Average performed correction of the MPTA, rotation and PPTA.

Performed MPTA correction (°) (Mean ± SD)	Performed rotation correction (°) (Mean ± SD)	Performed PPTA correction (°) (Mean ± SD)
7.34 + 0.08	9.98 + 0.20	10.00 + 0.07

6.2.2.3 MCW HTO

MCW HTO validation required ten new tibiae. The mean MPTA of these tibiae was 89.5 ± 0.9°. Mean tibial rotation was 34.3° ± 8.5° and mean PPTA was 81.8° ± 2.6°. Again, *Table 27 and 28* show the differences and performed corrections. MPTA correction accuracy was within 0.13°, PPTA correction accuracy within 0.09° and rotation correction accuracy within 0.20°. Mean correction accuracies were: MPTA 0.03° ± 0.04°, PPTA 0.01° ± 0.06° and tibial rotation 0.01° ± 0.03°. The histograms are shown in *Appendix A Figure 38*.

Table 27: The desired corrections in all three planes of the tibia and the average differences between the desired and achieved geometry.

MPTA correction (°)	Difference (°) (Mean ± SD)	Rotation correction (°)	Difference (°) (Mean ± SD)	PPTA correction (°)	Difference (°) (Mean ± SD)
Original – 7.0	0.03 ± 0.04	Original +/- 10.0	0.01 ± 0.03	Original +/- 10.0	0.01 ± 0.06

Table 28: Average performed correction of the MPTA, rotation and PPTA.

Performed MPTA correction (°) (Mean ± SD)	Performed rotation correction (°) (Mean ± SD)	Performed PPTA correction (°) (Mean ± SD)
-7.45 + 0.18	10.13 + 0.42	9.53 + 1.59

6.3 RESULTS PSI

For validation of the PSI algorithm ten PSI were developed. Two PSI were developed for each osteotomy type, excluding the LCW HTO. An example of a PSI for a LOW DFO can be seen in *Figure 30*. The algorithm required minimal user input. The user had to place the osteotomy plate, indicate the type of osteotomy, and draw a curve for the base of the PSI. All other steps in the design process were automated. This resulted in a mean design time of 01:49 min.

The PSIs were visually inspected on several requirements. First, the fit of the PSI on the bone was evaluated. Next, location and direction of the drill- and k-wire guides were evaluated. Furthermore, it was checked whether the hinge protecting k-wire intersected with one of the screws. Lastly, the location and direction of the sawguide were compared to the original sawplane. All these requirements were met by all PSIs.

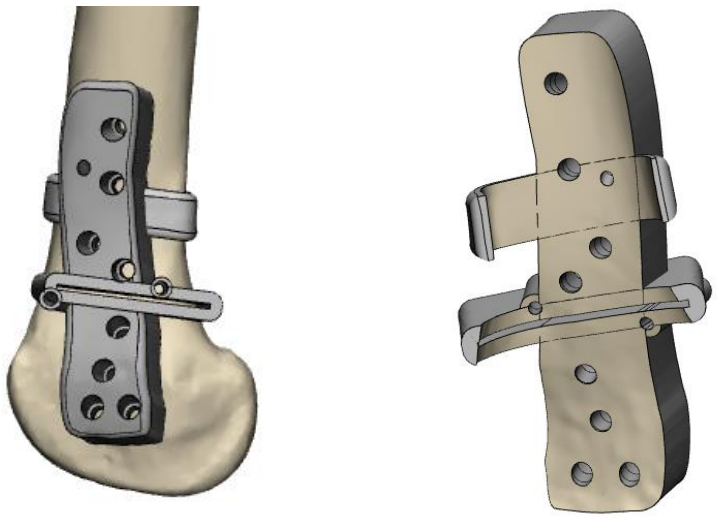

Figure 30: Front and back of a PSI for distal femoral lateral opening wedge osteotomy.

After visual inspection, several measurements were made to the PSI. First, the radius for the drill guides was measured. As shown in *Figure* 31 all radii were 3.00 mm as described in the requirements. The radii of the k-wires also corresponded with the requirements. Furthermore, the depth of holes was measured, using the measurement tools in 3-matic. Depths ranged from 9 – 11 mm. Lastly, the dimensions of the sawguide were evaluated, as shown in *Figure 31*. All PSI reached the dimensions as noted in the requirements.

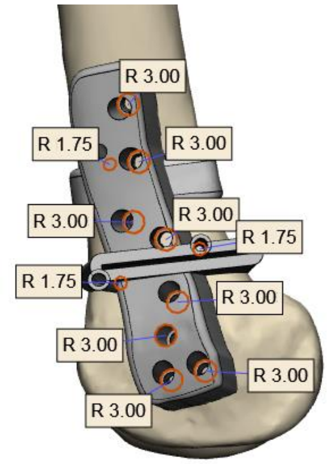

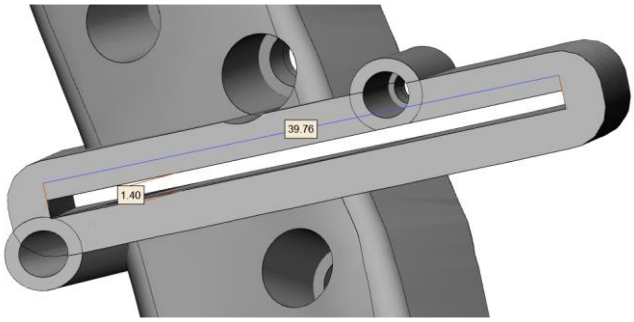

Figure 31: Measurements of the drill holes, k-wire guides and sawguide

7 VALORISATION

After validation of the deformity analysis and virtual osteotomy algorithm, several changes were made based on newly gained insights. First, the process around location of the posterior tibial points was adjusted, as these could not be found in some instances. This resulted in the algorithm to crash and not producing the angle measurements, despite most landmarks being found. When the algorithm does not find the posterior points, it lets the user indicate these points manually. These manually selected points are then used to produce the angle measurements.

Furthermore, validation of the femur virtual osteotomy algorithm showed that rotation correction accuracy could be improved. For this, another loop of rotation correction optimalisation was added to the algorithm. Previously, the algorithm would optimise the rotation correction, followed by varisation or valgisation. This correction of the mLDFA resulted in minor changes to the femoral rotation, which decreased accuracy. Therefore, the rotation correction loop was added again after mLDFA correction. This resulted in more accurate corrections and did not lead to noticeable longer run times.

Another problem of the femur virtual osteotomy was relocating the FLCD and FMCD. In some instances, the algorithm came in an infinite loop because of this. Therefore, the algorithm was adjusted to not relocate the distal landmarks.

In the design process of the PSI several considerations had to be made. The PSI uses surgical stainless-steel inserts for the drill guides and k-wire guides. These inserts were produced by the Medical Technology and Clinical Physics (MTKF) department of the UMCU. *Figure 32* shows the design of the drill guide and the k-wire guide inserts. After insert design, the ideal diameter of the drill guide holes in the PSI had to be determined. Three blocks with holes with increasing diameter were SLS printed. Furthermore, the holes had a distinctive design, which is displayed in *Figure 33.* After printing, the inserts were fitted into the holes. The 6.1 mm round hole resulted in the best fit, as it resulted in the insert not being able to wobble or rotate very easily.

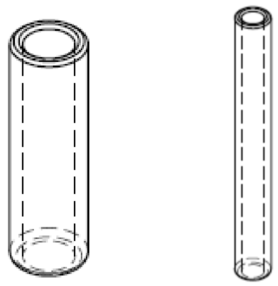

Figure 30: The left image shows the design of the drill guide. The right displays the k-wire guide.

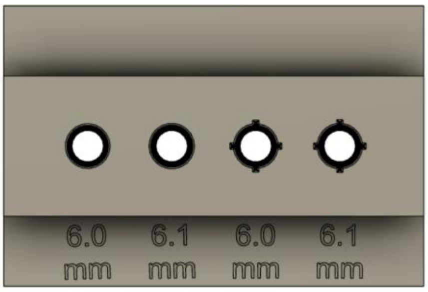

Figure 31: Design of one of the blocks used to find the optimal design for the drill holes of the PSI. The hole second from the left had the optimal design.

8 DISCUSSION

8.1 DISCUSSION DEFORMITY ANALYSIS

In this study, algorithms were developed for deformity analysis of the femur and the tibia. ICC calculations showed perfect agreement. The deformity analysis algorithms decreased the intra-observer variability as compared to manual deformity analysis. Visual inspection of manually versus software derived landmarks indicated better accuracy using the algorithm.

Manual landmark registration in the current study was less reliable when compared to Furmetz *et al.*.[47] Intra-observer variability in their study ranged between 0.6 mm to 4.6 mm, whereas this ranged between 0.6 mm to 8.9 mm in this study. Furthermore, Fürmetz used a different method to calculate the intra-observer precision. They conducted measurements three times and calculated a mean Euclidian distance to the mean position from three measurements. Lastly, the mean of this Euclidian distance was calculated to find the final intra-observer variability of each landmark. In our study, the Euclidian distances were directly between the landmarks. The method using mean positions automatically leads to lower intra-observer variabilities compared to the method of direct landmark comparison proposed in our study. Moreover, Fürmetz et al. reported interobserver variabilities between 0.22° and 5.25°, while the semi-automatic algorithm ranged between 0.09° to 0.97°. ICCs were similar between the two studies, except for the tibial rotation, where the present study reports an ICC of 0.987 as compared to an ICC of 0.69 reported by Fürmetz. This was expected, as posterior tibial points were hard to manually locate consistently. Furthermore, outliers were compared. Outliers of femoral deformity analysis were similar between the studies. However, a few outliers of tibial deformity analysis were higher in our study. This might be due to the larger amount of analysed lower limbs in our study, namely eighty versus six by Fürmetz *et al.*. Victor et al. conducted a study on intra- and interobserver variability in lower limb deformity analysis on CT-scans.[65] This study calculated variability by computing the Euclidian distances of a landmark to the mean location of this landmark. The study reported mean interobserver variability between 0.3 mm and 3.5 mm, comparable to the results obtained of the semi-automatic algorithm. In this study, variability was calculated with the same method as by Fürmetz. Furthermore, Subburaj *et al*. developed an algorithm for 3D deformity analysis, which achieved an accuracy of 1.9 mm to 4.9 mm.[66] The higher limit of this accuracy range was comparable to the higher limit found in this study. However, the lower boundary in our study was close to 0.1 mm, which was far below the lower limit of the algorithm developed by Subburaj *et al*..

As expected, the landmarks which required more manual input, had a higher variability (i.e., medial tuberosity, pcl-insertion, and epicondyles). However, this was not in range with the variability of the angles, which showed to be lower. This was probably because these landmarks were not being used directly in measurement of the angles, as these landmarks are only used to define the orientation of the coordinate system. Explanations for the higher variability observed for the LDTA and PPTA laid in the orientation of the distal tangent and the tibia plateau plane. Larger variabilities were observed in these landmarks, which directly corresponded to some of the angles of the tibia. Moreover, the distal tangent and tibia plateau plane were based on marking of the distal and proximal tibia plateau. As these were manual tasks, it could have resulted in the larger variability.

Furthermore, the accuracy of the algorithm was compared to the accuracy of the CT-scan. In this study the pixel size of the CT-scan were 0.98x0.98 mm and slice thickness was 1.0 mm. Observer variabilities for most landmarks were below this 1.0 mm range. However, not all measurements fell below this range. Nevertheless, the larger deviations seen in the landmarks of the femur, did not lead to large variability for the angles of the femur.

Comparing Euclidian distances of manual registration versus semi-automatic registration showed that these were in a comparable range to the manual intra-observer measurements. Therefore, to assess the accuracy of the algorithms, visual comparison of these landmark positions was required. This was necessary to assess the accuracy of the algorithms. Hence, the position of the corresponding landmarks was scored. This led to the conclusion that the software derived landmarks had a higher accuracy. A limitation to this method was that it is still very subjective due to visual analysis. Especially in the present study this could have had an influence on the results, as a single rater performed scoring. Further research should include more raters to reduce subjectivity.

A limitation of this study was that validation was performed on non-deformed legs. The choice for a healthy population was made, as no large database of deformed lower limbs was available and sample size calculation showed that a minimum of seventeen individuals was needed to validate the algorithm. Therefore, this was not completely representable for the intended patient population. Hence, deformity analysis was performed on five deformed femora and five deformed tibiae to get an impression of the performance of the algorithms on deformed lower limbs. Based on this, several adjustments were proposed to the algorithms as described in Chapter 7. However, as this sample of deformed lower limbs was so small, it cannot be ruled out that additional adjustments to the algorithm must be made, to create a functioning algorithm for all deformed lower limbs.

Furthermore, in the population with lower limb deformation, osteophytes are present around the knee. These osteophytes drastically influence the localisation of the landmarks, as the algorithm is not able to differentiate between osteophytes and regular bone. Therefore, the algorithm should also be validated on deformed lower limbs. Currently, if osteophytes are present, the user can manually relocate a landmark. Furthermore, the radius of the cylinder used to find the FCL and FCM cannot not be made larger than 5 mm, due to possible osteophytes which could affect landmark location. Therefore, this results in larger observer variabilities, due to manual input variabilities. Therefore, future research should add an option to exclude or remove osteophytes from the segmentation.

As mentioned in Chapter 7: valorisation, the algorithm was not able to locate all posterior tibial landmarks. Therefore, a work-around was created. Future research should focus on improving the localisation of these posterior landmarks, as these are directly used for calculation of the tibial rotation. Moreover, the algorithm could be further improved for localisation of the distal tangent of the tibia. Visual inspection showed that this line was often incorrect located. Therefore, the current method of marking the distal tibia should be replaced with a new method. An example of this could be using a curvature analysis. Further improvements could be made in locating the medial tuberosity and pcl-insertia, as these steps are still completely manual. This is also reflected in the high intra- and interobserver variability. These two landmarks were used to orientate the sagittal plane and could therefore have influenced measurement of the tibial slope.

Furthermore, future research may investigate the automated segmentation of lower limbs. Especially when volumes and speed of deformity analysis improves, segmentation will take most of the time. Currently, segmenting a lower limb takes 15-30 minutes depending on CT quality. Therefore, further investigation of automated segmentation can reduce the total time required to perform a deformity analysis. Also, future research could investigate the use of weight bearing CT-scans or artificially created weight bearing scans. The frontal plane knee alignment is influenced by weight bearing.[67] Therefore, angles like the HKA and Joint Line Convergence Angle (JLCA) cannot be measured by the deformity analysis algorithm. Hence, these angles must be measured on standard WLRs. To optimise the workflow, this could also be incorporated in the deformity analysis algorithm.

The algorithm reduces the intra- and interobserver variability as compared to manual deformity analysis. Furthermore, it increases reliability and repeatability and reduces the total time needed to perform deformity analysis. Therefore, it can contribute to current clinical practice. However, as not all landmarks can be located with a very high accuracy, it is suggested to perform visual inspection after application of the algorithm. Furthermore, future recommendations should be considered to further improve the algorithm.

8.2 Discussion virtual osteotomy

The present study outlined the development and validation of algorithms for virtual femoral and tibial osteotomies. These algorithms achieved high accuracies, with tibial osteotomy accuracies slightly better than the femoral osteotomy accuracies. Additionally, the algorithms reduced time of virtual osteotomy planning.

The mean correction accuracies indicated a very good accuracy as compared to the accuracy requirement in the coronal plane of approximately 0.45° as described by Jones *et al.*.[68] Furthermore, the mean accuracies of the virtual HTO algorithm were below 0.10°. The maximal achievable accuracy of the SLS-printer used for printing of the PSI is 0.10 mm which roughly corresponds to a 0.08° correction.[69] However, the mean accuracy of the DFO rotation correction does not fall within this range. This was due to the order of the performed corrections. The algorithm first performed a rotation correction, followed by a coronal plane correction. This coronal plane correction resulted in changes to the femoral rotation. As the algorithm does not re-evaluate the femoral rotation, a difference between desired and achieved rotational geometry arose. Therefore, it is proposed that future research should re-evaluate the femoral rotation after a coronal plane correction. After this further rotation corrections could be performed, which would result in even more accurate virtual distal femoral osteotomies.

One of the strengths of this study was that the algorithm required very little user input, namely: the desired geometry and the rough frontal plane location of the hinge. This minimal user input resulted in the variability of the newly achieved lower limb geometry being extremely low. Moreover, corrections were validated for all techniques in DFO and HTO surgery. This showed that accurate corrections can be performed in multiple planes at the same time.

A drawback of this study was that not all multi-planar corrections were validated for the tibia. The combination of a slope correction and a rotational correction was not validated. Nevertheless, it is expected that this combination can be achieved with a high accuracy, due to the high accuracies of these corrections when not combined. Moreover, a tibial correction in all three planes was not performed, as these corrections are barely performed in the clinic. Furthermore, a substantial reduction in time needed to perform the virtual osteotomy is achieved, as it only took 2-3 minutes to perform a virtual osteotomy with the new algorithm.

A limitation of this study was that validation was performed on a dataset of healthy subjects. Therefore, the dataset did not include patients with large deformities as normally present in the patient group which undergo osteotomies with the aid of a PSI. The decision to use healthy subjects was made as a large database of CT-scans and segmentations was available, as compared to the small dataset of patients with deformities. To investigate the performance and accuracy of the algorithm for the targeted patient population, ten virtual osteotomies were performed on segmentations of lower limb deformity patients. The algorithm was able to perform corrections in eight of the ten cases. However, in two cases the algorithm ended up in the infinite loop as mentioned in the chapter valorisation. After the proposed changes were made, the algorithm was able to perform the corrections. Furthermore, coronal plane correction of the tibia was only validated for roughly 7° varisation or valgisation. However, in clinical practice, larger corrections are often performed using PSI. As seen in the validation of the virtual femur osteotomy algorithm, larger corrections tend to have a less accurate outcome. Therefore, it is suggested to perform validation of larger corrections on a new dataset with large deformities.

Furthermore, this study briefly investigated the option of a variable hinge position in tibial osteotomies where a frontal and sagittal plane (slope) correction were combined, as it was hypothesized that this would lead to less stress on the hinge. An algorithm was developed which was able to create a variable hinge position. However, when the slope required an increase, which is most often the case, this led to an anterolateral position of the hinge. An anterolateral hinge position is difficult to achieve during surgery, as an anteromedial approach is used. Due to this approach, it is difficult to position the oscillating saw and osteotomes enough posteromedial to create the desired (anterolateral) hinge position. Future research could investigate different sawguide designs, which would aid in achieving this anterolateral hinge position.

8.3 Discussion PSI

The algorithm developed in this study was able to design PSIs for all types of HTO and DFO, excluding the LCW HTO. As the algorithm was able to make PSIs for ten bones, it showed to be robust. Most of the criteria as formulated in the requirements were met except for the ability to adjust during the design process. Furthermore, user input was reduced to a minimum, with the algorithm only requiring manual placement of the osteotomy plate and manual indication of the PSI base.

Strengths of this study include that the time required to develop a PSI was significantly reduced from around one hour to two minutes. This is due to the significant reduction of user input. A reduced development time also leads to a decreased lead time and a decreased cost. This faster lead time can also result in an increase of production scale. Furthermore, this minimal amount of user input resulted in a high reproducibility and reliability. Because most of the user input is standardized, the k-wires guide the oscillating saw will always parallel to the sawplane to provide optimal guidance. Furthermore, the hinge protecting k-wire goes through the optimal position. By standardizing all dimensions as noted in the design requirements, user errors can be ruled out. Therefore, this algorithm adds some quality control to the entire process. This added quality control in combination with validation of the entire design process, aids the UMCU in subjecting to the Medical Device Regulation (MDR). Moreover, the MDR requires technical documentation and clinical evaluation. The algorithms in this study can aid with faster and more accurate technical documentation.

Another advantage of this study was that first steps were taken in the design of stainless-steel inserts for the PSI. These inserts were made more accurately as compared to the previously used 3D-printed drill- and k-wire guides. This resulted in inserts with smaller tolerances which reduced wiggling of the drill and k-wires.

One of the weaknesses of the algorithm is that there are no checkpoints during the design process of the algorithm. These checkpoints were drafted as one of the requirements to examine the PSI at several moments during the design process, so necessary adjustments could be made. An example of a checkpoint could be after the design of the k-wire guides. Currently, a problem can rise with the location of the hinge protecting k-wire. If the k-wire intersects with one of the screws, it is located more medially, which can lead to a surgically unachievable medial location of the k-wire. Therefore, the user should be able to relocate the k-wire guide. Due to time limitations, it was impossible to incorporate these checkpoints into the algorithm. Further research should focus on including the checkpoints, as the user currently must restart the algorithm and make the adjustments accordingly.

Furthermore, the algorithm is not able to design PSI in case of an LCW HTO. Integrating this technique into the algorithm proved to be very time consuming. Because the number of times an LCW HTO is performed in the UMCU is extremely low, it was decided to make further improvements on the leg measurement and virtual osteotomy algorithm instead of the LCW HTO integration. However, as the

LCW HTO is performed in other hospitals, future research should focus on implementation of the PSI design for LCW HTO.

Another drawback of this study was that the algorithm was only validated for the design of ten PSIs, due to the small dataset of deformed lower limbs. This resulted in merely two PSIs per technique. In these ten instances, the PSIs were developed successfully. However, as this is a small sample size, it cannot be excluded that in some cases the design process could not be successful. Therefore, the algorithm should be assessed using a larger sample.

Future research should focus on the design of the inserts and the geometry of the holes in the PSI. In this study a first design was made for the inserts. A cylindrical shape was chosen for the inserts. However, one of the problems with this design is that during the drill, the insert could start to rotate. If this occurs, it is suggested to look further into different insert shapes, like a hexagonal or conical shape. This could prevent the insert from rotating in the PSI. Furthermore, the UMCU 3D printer batch accuracy should be investigated further, as the insert size should be consistent. Differences in dimensions between batches, could result in misfitting of the drill in the guide hole. Additionally, further research could focus on automatic placement of the osteotomy plate. This is currently user dependant and therefore requires most of the time in the design process. It was further observed that osteotomy plate location had a considerable influence on the design of the PSI. This was especially the case in the proximal-distal position of the plate. Deviations in this direction led to an overlap of the sawguide with the drill guides, which reduced the structural strength of the PSI. A possible solution for this is that the plates have a marking which would correspond with the location of the sawplane. This ensures that the osteotomy plate is positioned more accurately.

9 CONCLUSION

In this study the 3D-workflow for the use of 3D technology in osteotomies around the knee was protocolized and automated. This was achieved through the development of several algorithms used in deformity analysis, virtual osteotomy, and PSI design. The semi-automatic deformity analysis algorithm reduced the intra- and interobserver variability as compared to manual lower limb deformity analysis. Furthermore, the semi-automatic virtual osteotomy algorithm ensures that pre-operative planning for multiplanar corrections can be achieved with a high accuracy, only ranging up to a mean inaccuracy of 0.2°. Finally, the semi-automatic PSI development algorithm adds standardization and quality control to the entire process. Furthermore, it reduces the design process time and reduces lead times.

REFERENCES

1. Michael JWP, Schlüter-Brust KU, Eysel P. Epidemiologie, ätiologie, diagnostik und therapie der gonarthrose. *Dtsch Arztebl*. 2010;107(9):152-162. doi:10.3238/arztebl.2010.0152
2. Artrose | Cijfers & Context | Huidige situatie | Volksgezondheidenzorg.info. https://www.volksgezondheidenzorg.info/onderwerp/artrose/cijfers-context/huidige-situatie#node-prevalentie-en-aantal-nieuwe-gevallen-van-artrose-huisartsenpraktijk. Accessed September 6, 2021.
3. Artrose | Kosten | Volksgezondheid en Zorg. https://www.vzinfo.nl/artrose/zorguitgaven. Accessed March 29, 2022.
4. Sharma L. Osteoarthritis of the Knee. Solomon CG, ed. *https://doi.org/101056/NEJMcp1903768*. 2021;384(1):51-59. doi:10.1056/NEJMCP1903768
5. Hunter DJ, Bierma-Zeinstra S. Osteoarthritis. *Lancet*. 2019;393(10182):1745-1759. doi:10.1016/S0140-6736(19)30417-9
6. Perlman A, Fogerite SG, Glass O, et al. Efficacy and Safety of Massage for Osteoarthritis of the Knee: a Randomized Clinical Trial. *J Gen Intern Med*. 2019;34(3):379. doi:10.1007/S11606-018-4763-5
7. Dell'Isola A, Steultjens M. Classification of patients with knee osteoarthritis in clinical phenotypes: Data from the osteoarthritis initiative. *PLoS One*. 2018;13(1). doi:10.1371/JOURNAL.PONE.0191045
8. Georgiev T, Angelov AK. Modifiable risk factors in knee osteoarthritis: treatment implications. *Rheumatol Int 2019 397*. 2019;39(7):1145-1157. doi:10.1007/S00296-019-04290-Z
9. Liu X, Chen Z, Gao Y, zhang J, Jin Z. High Tibial Osteotomy: Review of Techniques and Biomechanics. *J Healthc Eng*. 2019;2019. doi:10.1155/2019/8363128
10. Sherman SL, Thompson SF, Clohisy JCF. Distal Femoral Varus Osteotomy for the Management of Valgus Deformity of the Knee. *J Am Acad Orthop Surg*. 2018;26(9):313-324. doi:10.5435/JAAOS-D-16-00179
11. Quirno M, Campbell KA, Singh B, et al. Distal femoral varus osteotomy for unloading valgus knee malalignment: a biomechanical analysis. *Knee Surgery, Sport Traumatol Arthrosc 2015 253*. 2015;25(3):863-868. doi:10.1007/S00167-015-3602-Z
12. Bellemans J, Colyn W, Vandenneucker H, Victor J. The Chitranjan Ranawat Award: Is Neutral Mechanical Alignment Normal for All Patients?: The Concept of Constitutional Varus. *Clin Orthop Relat Res*. 2012;470(1):45. doi:10.1007/S11999-011-1936-5
13. Weinstein SL, Flynn JM. Lovell and Winter's Pediatric Orthopaedics. In: *Lovell and Winter's Pediatric Orthopaedics*. ; 2013:2544. www.ncbi.nlm.nih.gov/omim. Accessed July 4, 2022.
14. Knock Knees? - Can they be straightened without surgery? https://boroondaraosteopathy.com.au/knockknees/. Accessed April 6, 2022.
15. Thienpont E, Schwab PE, Cornu O, Bellemans J, Victor J. Bone morphotypes of the varus and valgus knee. *Arch Orthop Trauma Surg 2017 1373*. 2017;137(3):393-400. doi:10.1007/S00402-017-2626-X
16. Zampogna B, Vasta S, Amendola A, et al. Assessing Lower Limb Alignment: Comparison of Standard Knee Xray vs Long Leg View. *Iowa Orthop J*. 2015;35:49. /pmc/articles/PMC4492139/. Accessed September 8, 2021.
17. Cherian JJ, Kapadia BH, Banerjee S, Jauregui JJ, Issa K, Mont MA. Mechanical, Anatomical, and Kinematic Axis in TKA: Concepts and Practical Applications. *Curr Rev Musculoskelet Med*. 2014;7(2):89. doi:10.1007/S12178-014-9218-Y
18. Marques Luís N, Varatojo R. Radiological assessment of lower limb alignment. *EFORT Open Rev*. 2021;6(6):487-494. doi:10.1302/2058-5241.6.210015
19. Moreland JR, Bassett LW, Hanker GJ. Radiographic analysis of the axial alignment of the lower extremity. *J Bone Jt Surg - Ser A*. 1987;69(5):745-749. doi:10.2106/00004623-198769050-00016

20. DIAGNOSTIC CASE THREE: The Use of EOS to Assess Leg Length — Complex Hip Surgery. https://www.complexhipsurgery.com/diagnostic-case-three. Accessed April 6, 2022.
21. Paley D, Herzenberg JE, Tetsworth K, McKie J, Bhave A. Deformity planning for frontal and sagittal plane corrective osteotomies. *Orthop Clin North Am*. 1994;25(3):425-465. doi:10.1016/S0030-5898(20)31927-1
22. Maslaris A, Brinkmann O, Bungartz M, Krettek C, Jagodzinski M, Liodakis E. Management of knee dislocation prior to ligament reconstruction: What is the current evidence? Update of a universal treatment algorithm. *Eur J Orthop Surg Traumatol 2018 286*. 2018;28(6):1001-1015. doi:10.1007/S00590-018-2148-4
23. Dean RS, Larson CM, Waterman BR. Posterior Tibial Slope: Understand Bony Morphology to Protect Knee Cruciate Ligament Grafts. *Arthroscopy*. 2021;37(7):2029-2030. doi:10.1016/J.ARTHRO.2021.05.006
24. Driban JB, Stout AC, Duryea J, et al. Coronal tibial slope is associated with accelerated knee osteoarthritis: data from the Osteoarthritis Initiative. *BMC Musculoskelet Disord 2016 171*. 2016;17(1):1-7. doi:10.1186/S12891-016-1158-9
25. Çakmak M, Cıvan M. Sagittal Plane Deformities and Malorientation Test. *Basic Tech Extrem Reconstr Extern Fixator Appl Accord to Ilizarov Princ*. January 2018:267-275. doi:10.1007/978-3-319-45675-1_20
26. Schröter S, Elson DW, Ateschrang A, et al. Lower Limb Deformity Analysis and the Planning of an Osteotomy. *J Knee Surg*. 2017;30(5):393-408. doi:10.1055/s-0037-1603503
27. Farinelli L, Baldini M, Bucci A, Ulisse S, Carle F, Gigante A. Axial and rotational alignment of lower limb in a Caucasian aged non-arthritic cohort. *Eur J Orthop Surg Traumatol 2020 312*. 2020;31(2):221-228. doi:10.1007/S00590-020-02763-7
28. Häller TV, Schenk P, Jud L, Hoch A, Götschi T, Zingg PO. Consistency of 3D femoral torsion measurement from MRI compared to CT gold standard. *BMC Musculoskelet Disord*. 2021;22(1). doi:10.1186/S12891-021-04633-7
29. Scorcelletti M, Reeves ND, Rittweger J, Ireland A. Femoral anteversion: significance and measurement. *J Anat*. 2020;237(5):811. doi:10.1111/JOA.13249
30. Sabzevari S, Ebrahimpour A, Roudi MK, Kachooei AR. High Tibial Osteotomy: A Systematic Review and Current Concept. *Arch Bone Jt Surg*. 2016;4(3):204. /pmc/articles/PMC4969364/. Accessed September 7, 2021.
31. Woude JAD van der, Wiegant K, Heerwaarden RJ van, et al. Knee joint distraction compared with high tibial osteotomy: a randomized controlled trial. *Knee Surgery, Sport Traumatol Arthrosc*. 2017;25(3):876. doi:10.1007/S00167-016-4131-0
32. Prodromos CC, Amendola A, Jakob RP. High tibial osteotomy: indications, techniques, and postoperative management. *Instr Course Lect*. 2015;64:555-565. https://pubmed.ncbi.nlm.nih.gov/25745938/. Accessed September 8, 2021.
33. Mattei L, Lea S, Nicolaci G, Ferrero G, Marmotti A, Castoldi F. Closing wedge tibial osteotomy: is it an actual procedure nowadays? *Ann Jt*. 2017;2:30-30. doi:10.21037/AOJ.2017.06.04
34. Sun H, Zhou L, Li F, Duan J. Comparison between Closing-Wedge and Opening-Wedge High Tibial Osteotomy in Patients with Medial Knee Osteoarthritis: A Systematic Review and Meta-analysis. *J Knee Surg*. 2017;30(2):158-165. doi:10.1055/s-0036-1584189
35. Sherman SL, Thompson SF, Clohisy JCF. Distal Femoral Varus Osteotomy for the Management of Valgus Deformity of the Knee. *J Am Acad Orthop Surg*. 2018;26(9):313-324. doi:10.5435/JAAOS-D-16-00179
36. Jacobi M, Wahl P, Jakob RP. 4 Basic principles of osteotomies around the knee. In: *Osteotomies around the Knee*. Georg Thieme Verlag; 2014. doi:10.1055/b-0034-9884
37. Nguyen HC, Gielis WP, van Egmond N, et al. The need for a standardized whole leg radiograph guideline: The effects of knee flexion, leg rotation, and X-ray beam height. *J Cartil Jt Preserv*. 2021;1(3):100022. doi:10.1016/J.JCJP.2021.100022
38. Babazadeh S, Dowsey MM, Bingham RJ, Ek ET, Stoney JD, Choong PFM. The long leg radiograph is a reliable method of assessing alignment when compared to computer-assisted

navigation and computer tomography. *Knee*. 2013;20(4):242-249. doi:10.1016/J.KNEE.2012.07.009
39. Jamali AA, Meehan JP, Moroski NM, Anderson MJ, Lamba R, Parise C. Do small changes in rotation affect measurements of lower extremity limb alignment? *J Orthop Surg Res*. 2017;12(1):1-8. doi:10.1186/S13018-017-0571-6/TABLES/2
40. Van den Bempt M, Van Genechten W, Claes T, Claes S. How accurately does high tibial osteotomy correct the mechanical axis of an arthritic varus knee? A systematic review. *Knee*. 2016;23(6):925-935. doi:10.1016/J.KNEE.2016.10.001
41. Van Genechten W, Van Tilborg W, Van den Bempt M, Van Haver A, Verdonk P. Feasibility and 3D Planning of a Novel Patient-Specific Instrumentation Technique in Medial Opening-Wedge High Tibial Osteotomy. *J Knee Surg*. May 2020. doi:10.1055/s-0040-1710379
42. Jacquet C, Chan-Yu-Kin J, Sharma A, Argenson JN, Parratte S, Ollivier M. "More accurate correction using "patient-specific" cutting guides in opening wedge distal femur varization osteotomies. *Int Orthop*. 2019;43(10):2285-2291. doi:10.1007/s00264-018-4207-1
43. Fucentese SF, Meier P, Jud L, et al. Accuracy of 3D-planned patient specific instrumentation in high tibial open wedge valgisation osteotomy. *J Exp Orthop*. 2020;7(1). doi:10.1186/S40634-020-00224-Y
44. Jacquet C, Sharma A, Fabre M, et al. Patient-specific high-tibial osteotomy's 'cutting-guides' decrease operating time and the number of fluoroscopic images taken after a Brief Learning Curve. *Knee Surgery, Sport Traumatol Arthrosc*. 2020;28(9):2854-2862. doi:10.1007/s00167-019-05637-6
45. Lehmann CU, Miller MR. Standardization and the Practice of Medicine. *J Perinatol 2004 243*. 2004;24(3):135-136. doi:10.1038/sj.jp.7211060
46. Walter SD, Eliasziw M, Donner A, The JP. Sample size and optimal designs for reliability studies. *Stat Med*. 1998;17:101-110. doi:10.1002/(SICI)1097-0258(19980115)17:1
47. Fürmetz J, Sass J, Ferreira T, et al. Three-dimensional assessment of lower limb alignment: Accuracy and reliability. *Knee*. 2019;26(1):185-193. doi:10.1016/J.KNEE.2018.10.011
48. Radiopaedia - Drawing Femur anterior view - no labels | AnatomyTOOL. https://anatomytool.org/content/radiopaedia-drawing-femur-anterior-view-no-labels. Accessed April 7, 2022.
49. Diagram: Fibula and Tibia Labeling | Quizlet. https://quizlet.com/331071163/fibula-and-tibia-labeling-diagram/. Accessed April 7, 2022.
50. Folinais D, Thelen P, Delin C, Radier C, Catonne Y, Lazennec JY. Measuring femoral and rotational alignment: EOS system versus computed tomography. *Orthop Traumatol Surg Res*. 2013;99(5):509-516. doi:10.1016/J.OTSR.2012.12.023
51. Marx RG, Grimm P, Lillemoe KA, et al. Reliability of lower extremity alignment measurement using radiographs and PACS. *Knee Surgery, Sport Traumatol Arthrosc*. 2011;19(10):1693-1698. doi:10.1007/S00167-011-1467-3/TABLES/6
52. Yazdanpanah O, Mobarakeh MK, Nakhaei M, Baneshi MR. Comparison of Double and Single Leg Weight-Bearing Radiography in Determining Knee Alignment. *Arch Bone Jt Surg*. 2017;5(3):174. doi:10.22038/abjs.2017.20780.1538
53. Gaj E, Monaco E, De Carli A, et al. Measurement technique for posterior tibial slope on radiographs can affect its relationship to the risk of anterior cruciate ligament rupture. *Int Orthop*. 2021;45(6):1469-1475. doi:10.1007/S00264-020-04865-7
54. Jud L, Roth T, Roth T, et al. The impact of limb loading and the measurement modality (2D versus 3D) on the measurement of the limb loading dependent lower extremity parameters. *BMC Musculoskelet Disord*. 2020;21(1). doi:10.1186/S12891-020-03449-1
55. Kim TW, Lee MC, Cho JH, Kim JS, Lee YS, Md §. The Ideal Location of the Lateral Hinge in Medial Closing Wedge Osteotomy of the Distal Femur Analysis of Soft Tissue Coverage and Bone Density. doi:10.1177/0363546519869325
56. Akamatsu Y, Kobayashi H, Tsuji M, Nejima S, Kumagai K, Saito T. Should sagittal osteotomy line be parallel to tibial posterior slope in high tibial osteotomy? *BMC Musculoskelet Disord*.

2018;19(1):1-8. doi:10.1186/S12891-018-2257-6/FIGURES/6
57. Pape D, Lorbach O, Schmitz C, et al. Effect of a biplanar osteotomy on primary stability following high tibial osteotomy: A biomechanical cadaver study. *Knee Surgery, Sport Traumatol Arthrosc*. 2010;18(2):204-211. doi:10.1007/S00167-009-0929-3/TABLES/2
58. Presutti M, Goderecci R, Palumbo P, et al. A novel biplanar medial opening-wedge high tibial osteotomy: the Z-shaped technique. A case series at 7.2 years follow-up. *J Orthop Traumatol*. 2021;22(1):1-14. doi:10.1186/S10195-021-00617-4/FIGURES/10
59. Capella M, Gennari E, Dolfin M, Saccia F. Indications and results of high tibial osteotomy. *Ann Jt*. 2017;2:33-33. doi:10.21037/AOJ.2017.06.06
60. Tunggal JAW, Higgins GA, Waddell JP. Complications of closing wedge high tibial osteotomy. *Int Orthop*. 2010;34(2):255. doi:10.1007/S00264-009-0819-9
61. Kim MK, Ko BS, Park JH. The proper correction of the mechanical axis in high tibial osteotomy with concomitant cartilage procedures - A retrospective comparative study. *J Orthop Surg Res*. 2019;14(1):1-8. doi:10.1186/S13018-019-1333-4/FIGURES/4
62. *IO1-Methodology for Defining 3D Printing Exercises Suitable for Transversal Education*. https://www.e3dplusvet.eu/wp-content/docs/O1A1-EN.pdf. Accessed October 5, 2021.
63. Design guidelines for polymer parts produced with Selective Laser Sintering. www.oceanz.eu. Accessed October 25, 2021.
64. Activmotion high tibial osteotomy plates. *Brochure*. https://newcliptechnics.com/media/activmotion_brochure_incl_surgical_technique_1.pdf. Accessed October 25, 2021.
65. Victor J, Van Doninck D, Labey L, Innocenti B, Parizel PM, Bellemans J. How precise can bony landmarks be determined on a CT scan of the knee? *Knee*. 2009;16(5):358-365. doi:10.1016/J.KNEE.2009.01.001
66. Subburaj K, Ravi B, Agarwal M. Automated identification of anatomical landmarks on 3D bone models reconstructed from CT scan images. *Comput Med Imaging Graph*. 2009;33(5):359-368. doi:10.1016/J.COMPMEDIMAG.2009.03.001
67. Paternostre F, Schwab PE, Thienpont E. The difference between weight-bearing and non-weight-bearing alignment in patient-specific instrumentation planning. *Knee Surgery, Sport Traumatol Arthrosc*. 2014;22(3):674-679. doi:10.1007/S00167-013-2687-5/TABLES/3
68. Jones LD, Brown CP, Jackson W, Monk AP, Price AJ. Assessing accuracy requirements in high tibial osteotomy: a theoretical, computer-based model using AP radiographs. *Knee Surgery, Sport Traumatol Arthrosc*. 2017;25(9):2952-2956. doi:10.1007/S00167-016-4092-3/FIGURES/3
69. Tech Specs for the Fuse 1 SLS 3D Printer. https://formlabs.com/3d-printers/fuse-1/tech-specs/. Accessed June 24, 2022.

APPENDIX

APPENDIX A

The histograms of the corrections for the DFO and HTO.

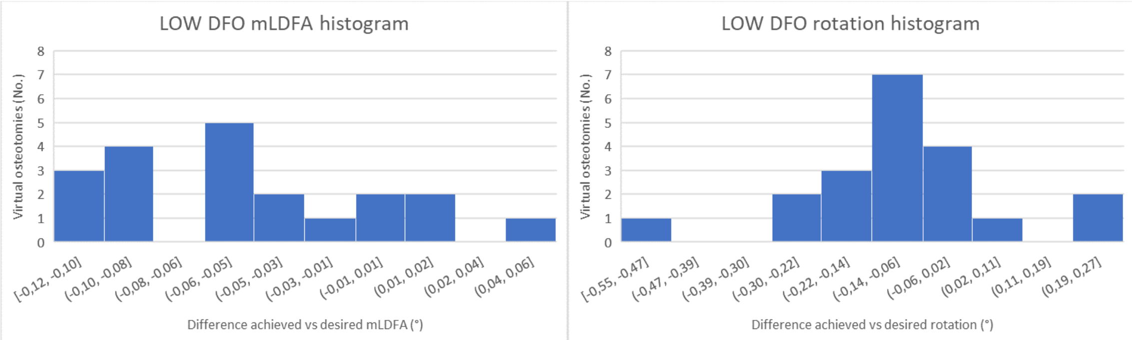

Figure 32: Histograms of differences between the achieved and desired mLDFA and rotation in virtual LOW DFO

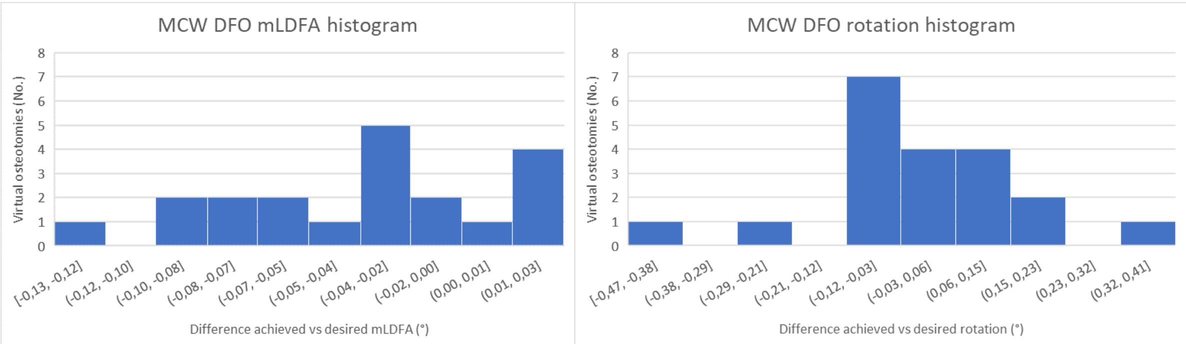

Figure 33: Histograms of differences between the achieved and desired mLDFA and rotation in virtual MCW DFO

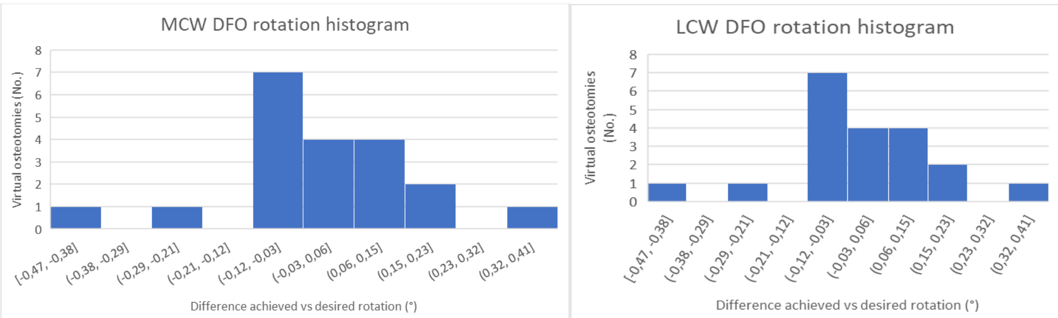

Figure 34: Histograms of differences between the achieved and desired mLDFA and rotation in virtual LCW DFO

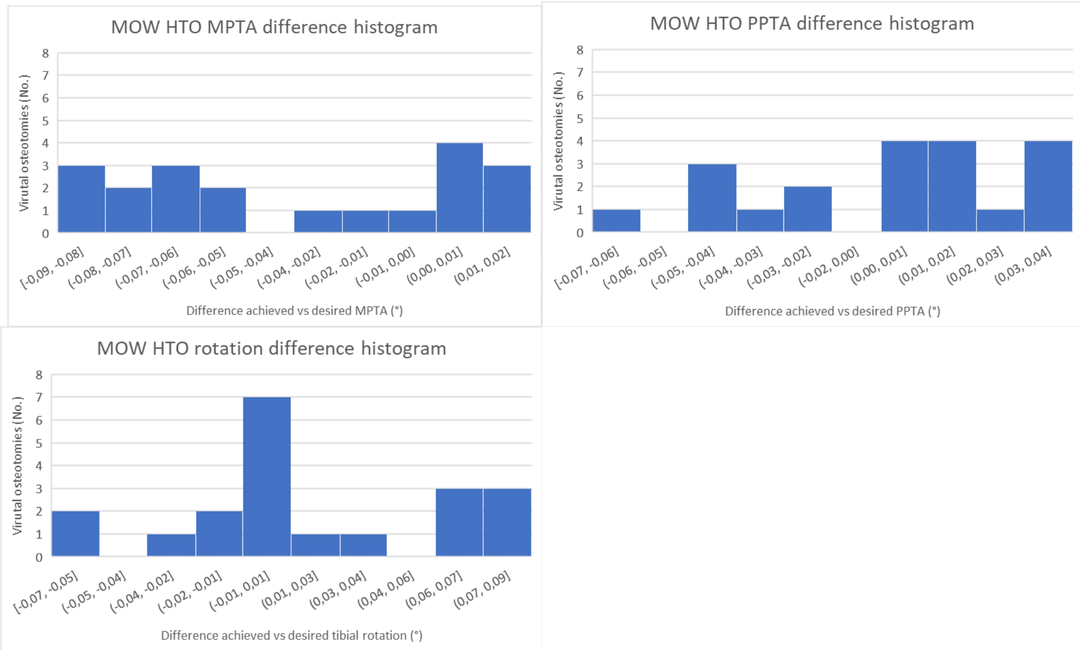

Figure 35: Histograms of differences between the achieved and desired MPTA, PPTA and rotation in virtual MOW HTO.

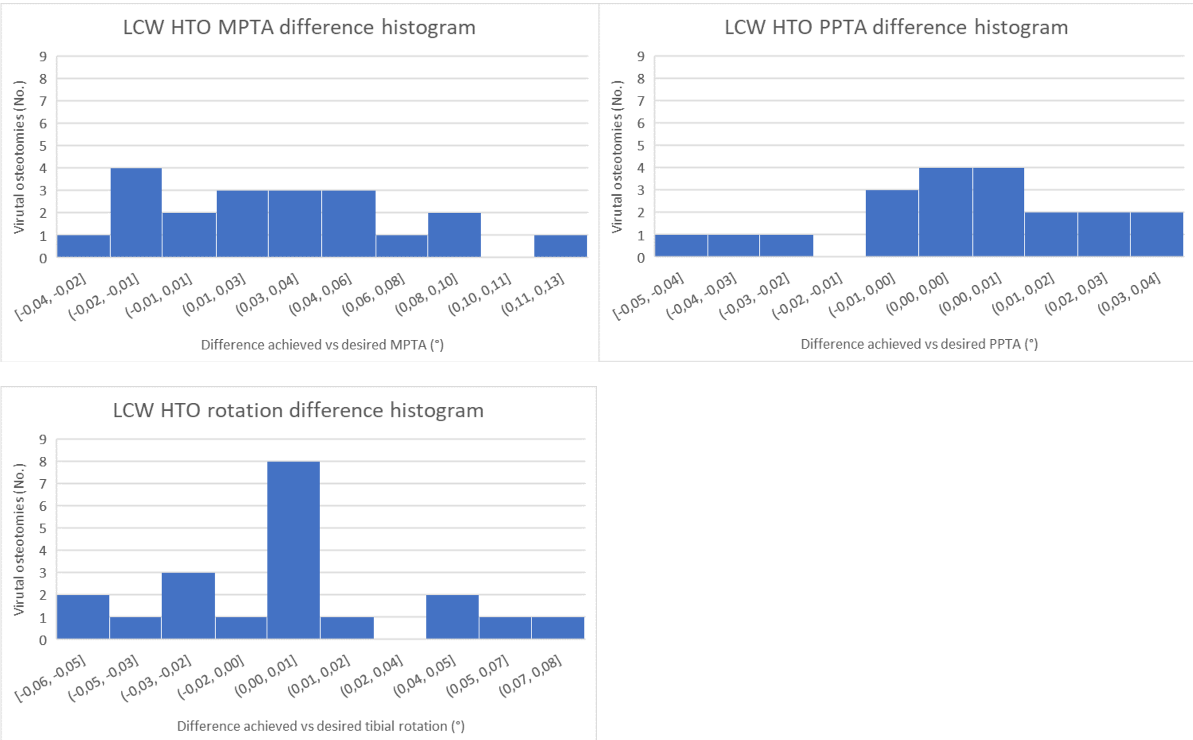

Figure 36: Histograms of differences between the achieved and desired MPTA, PPTA and rotation in virtual LCW HTO.

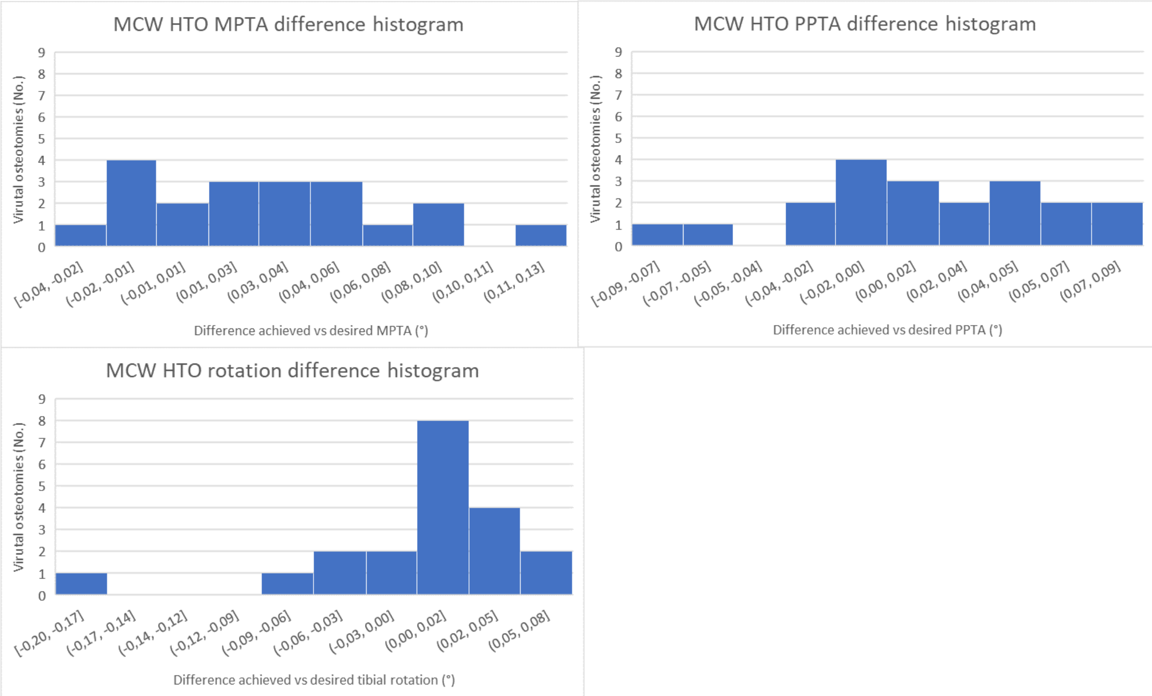

Figure 37: Histograms of differences between the achieved and desired MPTA, PPTA and rotation in virtual MCW HTO.